JANUARY 2024

M.Sc. in Materials Science and Engineering

MUHAMMED EL ACCEN

REPUBLIC OF TÜRKİYE

GAZİANTEP UNIVERSITY

GRADUATE SCHOOL OF NATURAL & APPLIED SCIENCES

SYNTHESIS OF ZINC OXIDE NANOSTRUCTURES BY CALCINATION AND SOLVOTHERMAL METHODS

M.Sc. THESIS

IN

MATERIALS SCIENCE AND ENGINEERING

BY

MUHAMMED EL ACCEN

JANUARY 2024

SYNTHESIS OF ZINC OXIDE NANOSTRUCTURES BY CALCINATION AND SOLVOLTHERMAL METHODS

M.Sc. Thesis

in

Materials Science and Engineering

Gaziantep University

Supervisor

Prof. Dr. Metin BEDİR

Co-Supervisor

Assoc. Prof. Dr. Derya KAPUSUZ YAVUZ

by

Muhammed EL ACCEN

January 2024

I hereby declare that all information in this document has been obtained and presented in accordance with academic rules and ethical conduct. I also declare that, as required by these rules and conduct, I have fully cited and referenced all material and results that are not original to this work.

Muhammed EL ACCEN

ABSTRACT

SYNTHESIS OF ZINC OXIDE NANOSTRUCTURES BY CALCINATION AND SOLVOTHERMAL METHODS

EL ACCEN, Muhammed
M.Sc. in Materials Science and Engineering
Supervisor: Prof. Dr. Metin BEDİR
Co-Supervisor: Assoc. Prof. Dr. Derya KAPUSUZ YAVUZ

January 2024

70 pages

This thesis includes a thorough examination into the synthesis and characterization of ZnO particles of various morphologies. The structure of the particles was analyzed by XRD, SEM, TEM, FTIR and XPS techniques and gas adsorption. XRD analysis confirmed the formation of wurtzite crystals, and microscopy images demonstrated their growth into various morphologies such as flower-like, nanorods, nanospheres, nanoprisms, and urchins. By XPS analysis, the oxygen defects on the particle surfaces were detected. The solvothermally produced nanospheres exhibited the highest mesopore surface area (30.56 m^2/g), while calcined nanorods had the lowest (4.55 m^2/g). The band gap energy (E_g) of the particles ranged between 3.08 and 3.29 eV and was lower than the theoretical value of wurtzite ZnO (3.37 eV). The photocatalytic degradation tests were carried out with methylene blue (MB) dye as the model organic pollutant. The results showed that calcined, acetic acid-modified nanorods were particularly ideal for photocatalytic degradation. Over the course of 24 h, 50.42 % of MB was degraded by these nanorods. Additionally, the thesis explored the preliminary experiments for the production and characterization of ZnO-PEG hybrids. FTIR spectra confirmed the interaction of PEG with ZnO on the particle surfaces. Their biocompatibility was qualitatively compared through immersion in simulated body fluid (SBF). Results revealed their potential to be used in the biomedical field.

Key Words: ZnO, Nanostructure, Photocatalytic, ZnO-PEG, Biocompatibility.

ÖZET

ÇİNKO OKSİT NANOYAPILARININ KALSİNASYON VE SOLVOTERMAL YÖNTEMLERLE SENTEZİ

EL ACCEN, Muhammed
Yüksek Lisans Tezi, Malzeme Bilimi ve Mühendisliği
Danışman: Prof. Dr. Metin BEDİR
İkinci Danışman: Doç. Dr. Derya KAPUSUZ YAVUZ

Ocak 2024

70 sayfa

Bu tez, çeşitli morfolojilerdeki ZnO parçacıklarının üretimi ve karakterizasyonunun kapsamlı bir incelemesini içermektedir. Parçacıkların yapısı, XRD, SEM, TEM, FTIR ve XPS teknikleri ve gaz adsorpsiyonu ile analiz edilmiştir. XRD analizi, vurtzit kristallerinin oluşumunu göstermiş olup ve mikroskopi görüntüleri, bunların çiçek benzeri, nanoçubuklar, nanoküreler, nano prizmalar ve kestaneler gibi çeşitli morfolojilere doğru büyüdüğünü açığa çıkarmıştır. XPS analizi ile parçacık yüzeylerindeki oksijen kusurları tespit edilmiştir. Solvotermal olarak üretilen nanoküreler en yüksek mezogözenek yüzey alanını (30,56 m^2/g) sergilerken, kalsinasyon yöntemi ile üretilen nanoçubukların en düşük (4,55 m^2/g) yüzey alanına sahip olduğu görülmüştür. Parçacıkların bant aralığı enerjisi (E_g) 3,08 ile 3,29 eV arasında değişmiştir ve vurtzit ZnO'nun teorik değerinden (3,37 eV) daha düşük elde edilmişlerdir. Fotokatalitik bozunma testleri, model organik kirletici olarak metilen mavisi (MB) boyası ile gerçekleştirilmiştir. Sonuçlar, kalsine edilmiş ve asetik asitle modifiye edilmiş nanoçubukların fotokatalitik bozunma için özellikle ideal olduğunu göstermiştir. 24 saat içinde MB'nin %50,42'si bu nanoçubuklar tarafından bozunmuştur. Ayrıca bu tezde ZnO-PEG hibritlerinin üretimi ve karakterizasyonuna yönelik ön deneyler yapılmıştır. FTIR spektrumları, parçacık yüzeyleri üzerinde PEG'in ZnO ile etkileşimini doğrulamıştır. Hibritlerin biyouyumlulukları, simüle edilmiş vücut sıvısına (SBF) daldırma yoluyla niteliksel olarak karşılaştırılmıştır ve sonuçlar bunların biyomedikal alanda kullanılma potansiyelini ortaya çıkarmıştır.

Anahtar Kelimeler: ZnO, Nanoyapı, Fotokatalitik, ZnO-PEG, Biyouyumluluk.

"Dedicated to my family"

ACKNOWLEDGEMENTS

I would like to thank my supervisor, Prof. Dr. Metin BEDİR, and my co-supervisor, Assoc. Prof. Dr. Derya KAPUSUZ YAVUZ for their guidance and support throughout the study. I am thankful for their encouragement and motivation.

I would like to express my love and gratitude to my family for their support.

TABLE OF CONTENTS

LIST OF TABLES

Page

LIST OF FIGURES

Page

LIST OF SYMBOLS

α	Alpha
β	Beta
ºC	Degree Celsius
∞	Infinity
λ	Lambda
θ	Theta

LIST OFABBREVIATIONS

AA	Acetic Acid
BJH	Barrett-Joyner-Halenda
BET	Brunauer-Emmet-Teller
DW	Deionized Water
DRS	Diffuse Reflectance Spectroscopy
EtOH	Ethanol
FTIR	Fourier Transform Infrared Spectroscopy
FWHM	Full Width at Half Maximum
IUPAC	International Union of Pure and Applied Chemistry
JCPDS	Joint Committee on Powder Diffraction Standards
K-M	Kubelka-Munk
LH	Langmuir-Hinshelwood
MB	Methylene Blue
PEG	Poly Ethylene Glycol
RS	Raman Spectroscopy
RT	Room Temperature
SBF	Simulated Body Fluid
NaOH	Sodium Hydroxide
SSA	Specific Surface Area
TEM	Transmission Electron Microscopy
UV	Ultra Violet
XRD	X-Ray Diffraction
XPS	X-ray Photoelectron Spectroscopy
ZAD	Zinc Acetate Dihydrate
ZnO	Zinc Oxide

CHAPTER 1
INTRODUCTION

1.1 Motivation

With the development of nanotechnology, a new age of materials science has begun, defined by an interdisciplinary approach that combines materials engineering with chemistry, physics, and biology to tackle difficult challenges in engineering applications. [1], [2]. Among the numerous materials investigated, zinc oxide (ZnO) appears as a versatile and attractive competitor for a variety of applications, particularly in the form of nanostructures and hybrids.

ZnO possesses intrinsic properties such as non-toxicity and antibacterial activity, which are indispensable for most medicinal applications. Moreover, its unique ability to interact with light through photocatalytic activities paves the way for advanced therapeutic and diagnostic techniques [3]. Furthermore, ZnO can be chemically modified using polymers for specific capabilities or morphologically for greater surface area [4]. For instance, ZnO-polymer hybrids stand at the forefront as potential materials for drug delivery systems [5]. They can be engineered to respond to various stimuli such as pH, temperature, or light, making them ideal for targeted drug release [5]. Furthermore, their high surface area and the ability to modify the surface with functional groups make them suitable carriers for therapeutic molecules [6]. Such smart delivery systems have the potential to transform the efficiency and accuracy of treatment modalities, particularly in the battle against cancer, where targeted delivery of chemotherapeutic drugs is important.

The synthesis of ZnO particles is an extensive research area and controllable synthesis of both ZnO and ZnO-polymer hybrid morphologies of large surface area is in high demand. Larger number of polymer or functional groups can interact with ZnO on its surface, providing not only more homogeneous and effective tailoring of the properties but also high loading capacity for i.e. Drugs. It also presents an opportunity to explore the interactions between inorganic nanoparticles and organic matrices, opens new avenues for research and applications [7].

In the overall, the synthesis of ZnO and its polymer hybrids is not only a response to the urgent needs for engineering applications, but also a stride toward the future of multifunctional materials. In this regard, the motivation for this work stems from its potential to make a substantial contribution to related research by exploiting the features of ZnO and ZnO-PEG to build innovative materials for engineering applications.

1.2 Scope and Objective of The Thesis

The scope of this thesis is to investigate the potential use of ZnO and ZnO-PEG hybrids for photocatalytic and biomedical applications. Thus, the general objective of the thesis is to synthesize distinct ZnO morphologies and then forming their hybrids with PEG, and investigate their photocatalytic capability and apatite-forming. Particular attention was paid to the correlation between the morphological characteristics of ZnO particles and their photocatalytic activity, with the aim of identifying those configurations that demonstrate superior performance.

In the light of this general objective, the specific goals are:

- Synthesis of distinct morphologies at low temperature and high impurity.
- Building a correlation between the structure and photocatalytic capability.
- Investigation of PEG-hybridization on the structure and Biocompatibility.

CHAPTER 2
LITERATURE REVIEW

2.1 Structure and Synthesis of ZnO Nanoparticles

ZnO stands as a semiconductor material that has captivated academic interest, largely attributable to its wide band gap and large exciton binding energy, properties that render it an exceptional candidate for using in electronic and optoelectronic devices [8]. It has three polymorphs: the stable phase; wurtzite [9], the zinc blende structure which is stable only when grown on cubic substrates [10], and the rock salt structure, which can be obtained at relatively high pressures [11] as shown in Figure 2.1.

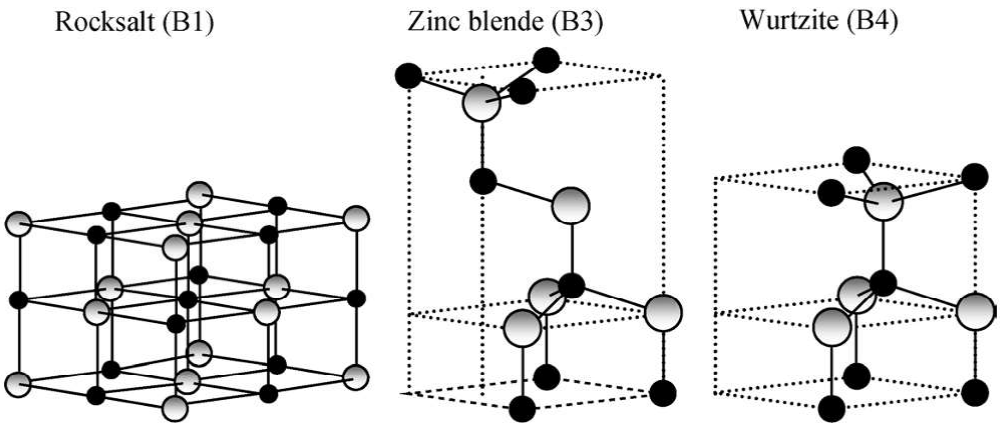

Figure 2.1. The three crystalline polymorphs of ZnO [12]

The semiconducting nature of ZnO, along with its environmental robustness and thermal stability, makes it an ideal candidate for applications in harsh operating conditions, where organic semiconductors might falter [13]. In the domain of transparent electronics, ZnO's ability to conduct electricity while maintaining transparency is leveraged in the fabrication of transparent conductive oxides [14], a critical component in liquid-crystal displays, touch screens, and solar cells. Furthermore, the high electron mobility of ZnO contributes to its efficiency in electronic transport, enhancing the performance of electronic devices [15].

The study and application of ZnO in the form of nanoparticles has a multifaceted history, marked by extensive research into its intrinsic properties and the pursuit of innovative synthesis techniques. ZnO nanoparticles are characterized by their distinctive physical and chemical attributes, which include a substantial band gap of approximately 3.37 eV and an exciton binding energy on the order of 60 milli-electron volts [16], [17], [18]. These features confer upon ZnO nanoparticles the capacity for absorbing ultraviolet light, thereby qualifying them as suitable agents for photocatalytic processes, a quality that has been harnessed in environmental remediation efforts [19], [20].

Historically, the development of ZnO nanoparticle synthesis has undergone significant advancements over time. Initially, synthesis techniques largely depended on vapor phase transport methods. These early methods were effective in producing nanoparticles but were also characterized by their intensive energy requirements and the need for high thermal inputs [21], [22]. Several novel chemical methods have been developed throughout time as the focus on energy efficiency and precise control over nanoparticle properties intensified. The sol-gel procedure is one of the most well-known and widely used processes [23].

The comparatively moderate synthesis conditions and high degree of homogeneity that the sol-gel procedure provides to the resultant nanoparticles made it a popular technology. Over time, the focus on energy economy and precise control over nanoparticle properties grew, leading to the development of several innovative chemical techniques. One remarkable technique that has gained traction is the sol-gel procedure [24]. This method involves the transition from a colloidal solution to a gel phase, culminating in the formation of ZnO nanoparticles whose size and crystallinity can be finely tuned, thereby enabling a direct correlation between synthesis conditions and photocatalytic activity [25].

The precipitation method for synthesizing ZnO nanoparticles is a strategic approach that involves the co-precipitation of zinc ions with a precipitating agent to form ZnO, and this technique stands out for its simplicity and cost-effectiveness, which make it highly attractive for large-scale production [26]. The final step often involves calcination, where the dried zinc hydroxide is heated at elevated temperatures in a furnace to decompose it into ZnO [27]. This thermal treatment not only removes any

remaining organic or inorganic impurities but also leads to the formation of nanoparticles with a more defined crystalline structure and increased photocatalytic activity [27], [28].

Concurrently, solvothermal and hydrothermal synthesis have gained recognition for their lower operating temperatures, which generally do not surpass 250 ºC [29]. This approach facilitates the creation of ZnO nanoparticles with diverse morphologies [30], such as nanorods, nanowires, and nanoflowers, each morphology bringing its own set of surface characteristics and reactive facets to the fore, thus influencing photocatalytic efficiency.

The evolution of ZnO nanoparticle synthesis is reflective of a maturing synergy between disciplines such as material science, chemistry, and environmental engineering. This synergy is guided by the dual objectives of advancing material properties to suit targeted applications and adhering to the principles of green chemistry, which prioritize environmental sustainability alongside technological progress.

2.2 Photocatalytic Activity

Zinc Oxide (ZnO) is a widely studied photocatalyst due to its abundant availability, non-toxicity, and high photocatalytic efficiency under UV light [31]. Its high exciton binding energy is beneficial for photocatalytic applications because it allows efficient electron-hole pair separation, a crucial factor for photocatalytic processes [32].

ZnO's photocatalytic activity primarily involves the generation of electron-hole pairs upon UV light irradiation [33] as shown in Figure 2.2. These electron-hole pairs interact with water molecules or hydroxide ions to produce hydroxyl radicals, which are potent oxidizing agents capable of degrading a wide range of organic pollutants [34]. Additionally, the electrons can reduce oxygen molecules to form superoxide anions, further contributing to the degradation process [35], then by the reaction given in Eq. (2.1).

The photocatalytic efficiency of ZnO is influenced by several factors, including its morphology, crystal structure, surface area, and the presence of defects [36], [37]. Distinct morphologies of ZnO, such as nanoparticles, nanorods, and nanosheets, exhibit different photocatalytic activities due to their varying surface areas and crystal

facets [38]. The presence of defects can also significantly enhance photocatalytic activity by creating additional energy levels within the band gap or facilitating charge separation [39].

While ZnO is highly efficient under UV light, its application under visible light is limited due to its wide band gap [40]. Recent studies have focused on modifying ZnO with metal or non-metal doping, forming composites with other semiconductors, or sensitizing with organic dyes to extend its absorption to the visible light range [41].

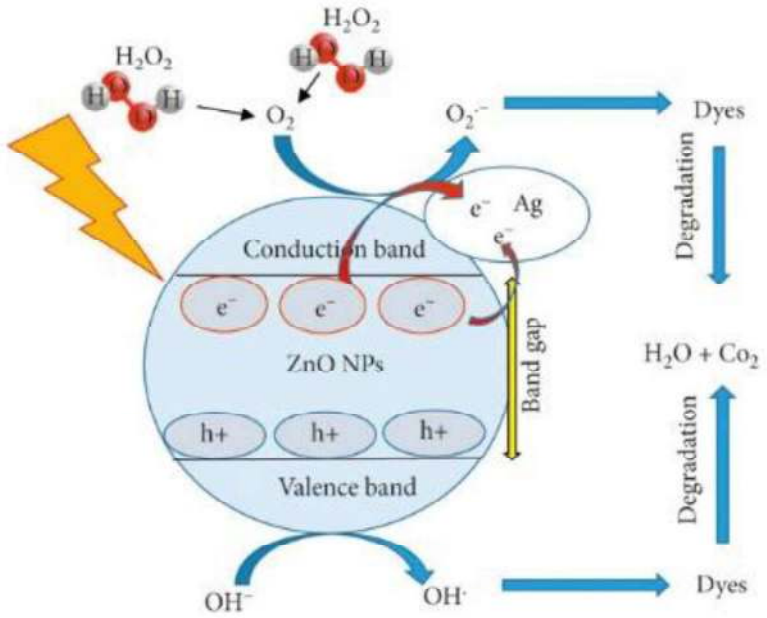

Figure 2.2. The proposed photocatalytic mechanism of ZnO nanostructures

The reaction of photocatalytic mechanism is shown in the Eq. (2.1):

$$ZnO + hv = ZnO^* + h^+ + e^- \qquad (2.1)$$

Where, hυ is the photon (light), ZnO^* is the excited state of ZnO, h^+ is the positive hole, and e^- is the free electron.

In summary, ZnO is a promising photocatalyst with considerable potential in environmental remediation, particularly in the degradation of organic pollutants. Ongoing research focuses on enhancing its efficiency, stability, and visible light activity to expand its applicability.

2.3 Hybridizing with Polymers and Biomedical Applications

The utilization of polymer coatings on nanoparticles has become increasingly prevalent in enhancing the functionality and application scope of nanomaterials. This approach involves encapsulating nanoparticles with polymers to improve their stability, biocompatibility, and functionality [42]. Among various polymers, Polyethylene Glycol (PEG) has gained significant attention due to its unique properties, such as water solubility and non-toxicity, which make it ideal for biomedical applications [43].

Focusing on PEG's application in coating ZnO nanoparticles, there's a synergy between the two materials that broadens their application potential. ZnO, known for its photocatalytic, antimicrobial, and UV-blocking properties, when coated with PEG, shows enhanced dispersion in aqueous and biological environments, and improved biocompatibility. This makes PEG-coated ZnO nanoparticles particularly suitable for drug delivery and wound healing [44].

Coating ZnO nanoparticles with PEG typically involves the attachment of PEG chains onto the ZnO surface, which can be achieved through various chemical methods. This process not only stabilizes the nanoparticles but also imparts new properties, such as increased hydrophilicity and reduced cytotoxicity [45].

In the realm of biomedical research, the interaction of PEG-coated ZnO nanoparticles with biological environments such as Simulated Body Fluid (SBF) is of particular interest. SBF tests are crucial for evaluating the bioactivity and biocompatibility of materials intended for medical use. These tests simulate the conditions of human body fluids, providing insights into how materials behave in a physiological environment [46]. PEG-coated ZnO nanoparticles, when tested in SBF, exhibit several notable behaviors that underscore their potential in biomedical applications. The interaction of these nanoparticles with SBF often results in the formation of a biomimetic apatite layer on their surface, indicative of good bioactivity and potential for bone tissue engineering [47].

Overall, the use of PEG-coated ZnO nanoparticles in SBF tests has provided valuable insights into their interaction with biological systems, paving the way for their use in a range of biomedical applications.

CHAPTER 3
EXPERIMENTAL PROCEDURE

3.1 Materials

Materials used in this work were of analytical grade and used without further purification. For the synthesis of ZnO, zinc acetate dihydrate (ZAD, ISOLAB 996.016, 99.5%, $Zn(CH_3COO)_2.2H_2O$) was used as the zinc precursor. Ethanol (EtOH, ISOLAB 920.026, 99.9%, C_2H_5OH) was used as the solvent for the solvothermal reaction. NaOH (NaOH, ISOLAB 969.11, 99%) and acetic acid (AA; TEKKIM TK010040.01001, 80%, CH_3COOH) were used as precipitating agents. For testing of photocatalytic capability, methylene blue (CHEMBIO CB2700.0100, $C_{16}H_{18}ClN_3S$) was used as the model organic pollutant. Deionized water (DW) was used for synthesis and in all washing procedures.

For coating of the ZnO structures produced, poly ethylene glycol (PEG, MERCK 25322-68-3, $(CH_2OH)_2$) was used. The biocompatibility tests were conducted using simulated body fluid (SBF). SBF was prepared using the formulation given on Table 3.1, as reported by Kokubo et *al*. [48].

Table 3.1. The chemical composition of SBF solution [Kokubo ref]

Order of Addition	Reagent	Chemical Formula	Purity %	Amount
1	Sodium Chloride	NaCl	99.5	8.035 g
2	Sodium Hydrogen Carbonate	$NaHCO_3$	99.5	0.355 g
3	Potassium Chloride	KCl	99.5	0.225 g
4	di-Potassium Hydrogen Phosphate	$K_2HPO_4.3H_2O$	99.0	0.231 g

5	Magnesium Chloride Hexahydrate	$MgCl_2.6H_2O$	98.0	0.311 g
6	1 M Hydrochloric Acid	HCl	-	39 ml
7	Calcium Chloride	$CaCl_2$	98.0	0.292 g
8	Sodium Sulfate	Na_2SO_4	99.0	0.072 g
9	Trizma Base	$(CH_2OH)_3CNH_2$	99.0	6.118 g
10	Sodium Chloride	NaCl	99.5	8.035 g

*Where 1 M HCl was used extra for pH adjustment (between 0 – 5 ml). pH value should be 7.25.

3.2 Synthesis of ZnO Nanoparticles

3.2.1 Synthesis by Calcination

For the synthesis of ZnO by calcination, products were first precipitated in solution, where work performing by S. Rani et *al* [49] was used as a reference study for the synthesis. Typically, the procedure of precipitation started by mixing 0.01 M (2.19 g) of ZAD with 10 ml of EtOH in a clean pot, then 0.05 M (2 g) of NaOH was added to the pot with 5 ml of DW for NaOH dissolving.

The mixture was then kept at RT for 15 min, then at 80 ºC for 45 min under continuous stirring. The precipitates were separated by centrifuging for 20 min, then drying in an oven at 80 ºC for 4 h. After drying, products were calcined at 200, 400, 600 ºC for 2 h. AA was added as the final step of an identical procedure to the samples designated as “2”. The synthesized sample formulations are listed on Table 3.2.

Note: All the results of samples (1a, 1b, 1d) and samples (2a, 2b, 2d) are not shown in this thesis, because they were identical to the results of the samples 1c and 2c which were chosen.

Table 3.2. Samples formulations for calcination

Sample Code	ZAD (g)	EtOH (ml)	NaOH (g)	DW (ml)	AA (ml)	Calcination Temperature (°C)	Time (h)
1a	2.19	10	2	5	-	-	2
1b						200	
1c						400	
1d						600	
2a	2.19	10	2	5	2	-	2
2b						200	
2c						400	
2d						600	

3.2.2 Solvothermal Synthesis

For samples 3 and 4, the solvothermal technique was used to produce ZnO products, as described in Section 3.2.1. After 4 h of stirring at 80 °C, the solution was transferred to a Teflon-lined stainless-steel reactor (50 mL) and exposed to a solvothermal reaction at 250 °C for 4 h. Following the completion of the reaction, the solution was vacuum-filtered using 0.22 μm filter paper. The ZnO precipitates were then dried for 4 h at 80 °C. Solutions in samples labeled "5" were subjected to solvothermal reactions at lower temperature for a longer period of time (24 h). The solution preparation technique was identical to that used in steps 3 and 4, but the formulas were different. The NaOH and AA additions were skipped in 5a and 5b, and DW was employed as the solvent instead of ethanol in 5c. Table 3.3 lists all of the solvothermal sample formulations.

Table 3.3. Samples formulations for solvothermal

Sample Code	ZAD (g)	EtOH (ml)	NaOH (g)	DW (ml)	AA (ml)	Solvothermal Temperature (ºC)	Time (h)
3	2.19	10	2	5	-	250	4
4	2.19	10	2	5	2	250	4
5a	2.5	25	-	-	-	200	24
5b	2.5	25	-	-	-	120	24
5c	0.62	-	2.4	30	-	100	24

3.3 Preparation of ZnO-PEG Hybrids

Based on their microstructural properties, four ZnO samples (2c, 3, 5b, 5c) were chosen for the preparation of ZnO-PEG hybrids. In a typical process, 0.11 g (0.1 ml) of PEG added in 50 ml of DW, then mixed with 50 mg of ZnO. The mixture was stirred at RT for 3 h, then centrifuged for 15 min to separate the particles. Particles were then washed with EtOH and dried at 60 ºC for 2 h. The formulations are summarized on Table 3.4.

Table 3.4. Formulations of ZnO-PEG hybrids

Sample Code	ZnO (g)	PEG (ml)	DW (ml)
(2c)-PEG (3)-PEG (5b)-PEG (5c)-PEG	0.05	0.11	50

3.4 Characterization and Testing

3.4.1 XRD Analysis

XRD analysis was carried out by scanning the ZnO particles in 10-90º 2-theta range, with Copper K-α monochromatic radiation (λ = 1.54056 Å), using Bruker D8 equipment. Particles were scanned with a rate of 2º/min. Using the Unit cell® software, the lattice properties of each composition were calculated. In addition, the average crystallite sizes were calculated using the Debye-Scherer Formula, shown in Eq. (3.1).

$$D = \frac{k\lambda}{\beta cos\theta} \qquad (3.1)$$

Where D is the crystallite size (nm), k is Scherer constant = 0.9, λ is the wavelength of the monochromatic X-ray (0.15406 nm for Cu-Kα), β is the full width at half maximum (FWHM in radians) of the peaks in 10-60° range used in the calculation and θ is the Bragg's angle in Radians [50].

3.4.2 Microscopy Analysis (SEM, TEM)

The morphology of ZnO particles was investigated using SEM (FEI Nova Nano SEM 430) operated at 20 kV voltage. Before the analysis, particles were dispersed on carbon tape and sputter-coated with Au/Pd. Particles were further analyzed by transmission electron microscope (TEM, JEOL 2100 RTEM) at 200 kV. Prior to TEM analysis, they were dispersed in EtOH and sonicated for 20 min for the aggregates to break down. Then a drop was taken from the EtOH surface and placed onto the carbon TEM grid.

3.4.3 Spectroscopic Analysis (FTIR, XPS)

For identifying the chemical structure, FTIR spectroscopy was performed using Shimadzu IRTracer-100 FTIR spectrometer. The spectral resolution was 4 cm^{-1} and each scan was performed in 4000 - 400 cm^{-1} range. To further characterize the chemical structure of the particle surfaces, X-ray photoelectron spectroscopy (Specs Flex XPS) with XRD 50 source at an excitation energy of 1486 eV was used to investigate the Zn and O bonding on the particle surfaces.

3.4.4 Gas Adsorption

To characterize the surface structure of samples, N_2 gas adsorption was performed using Micrometrics 3Flex Tristar II 3020 system equipped with BET analyzer. By the systems' software, adsorption isotherms, and average pore sizes were calculated using Barrett-Joyner-Halenda (BJH) approach. Before the analysis, particles were degassed at 80°C for 10h.

3.4.5 Energy Band Gap Determination

A UV-Visible spectrophotometer (Shimadzu UV-3600 Plus) was used to analyze and characterize the band gap structure of the particles. Scanning was performed in diffuse reflectance mode. Based on Eq. (3.2), Tauc method was used to calculate the direct band gap energy (E_g) [51].

$$(\alpha * h\upsilon)^{1/n} = B\ (h\upsilon - E_g) \qquad (3.2)$$

Where h is the Planck Constant, υ is the frequency of the photon, B is a constant to define the type of electron transition, and for direct transition band gaps, n equals 1/2.

Through the application of the Kubelka-Munk (K-M) theory, the DRS spectra of particles are collected and transformed to the absorbance spectra Eq. (3.3).

$$F(R\infty) = \frac{K}{S} = \frac{(1-R\infty)^2}{2R\infty} \qquad (3.3)$$

Where R is the reflectance of a specimen that is infinitely thick, S is the scattering coefficient, and K is the absorbance. According to K-M Theory, the equation can be modified to Eq. (3.4) by substituting F (R∞) with α:

$$(F(R\infty) * h\upsilon)^{1/n} = B\left(h\upsilon - E_g\right) \qquad (3.4)$$

The DRS scans were conducted in the 200–800 nm wavelength range to determine E_g, and Eq. (3.4) was applied. Each sample was plotted using the Tauc Plot ($F(R\infty) * h^{(1/n)}$ versus photon energy (h)), where n is 1/2. The x-axis was extended to include the steep, linear portions of the curves, and their intersection locations were noted as the direct E_g. The software Origin Pro® was used to extend the linear portion of the curves.

3.4.6 Photocatalytic Degradation Testing

In photocatalytic degradation experiments, MB was used as a model dye. The photocatalytic degradation capability of the ZnO particles was investigated under UV light irradiation. In a typical testing procedure, an aqueous MB solution ($MB_{(aq)}$) was prepared at 25 mg/L concentration. 50 mg of ZnO sample was added into 50 ml of $MB_{(aq)}$. Based on the analysis results and their microstructural properties, 7 samples were chosen for testing (1c – 2c – 3 – 4 – 5a – 5b – 5c).

In a typical test, ZnO containing $MB_{(aq)}$ was placed in a dark box and stirred at 500 rpm at RT. After 30 min of dark stirring, at specific time intervals, the UV-C lamp (8 W, 365 nm, OSRAM) in the box was switched on and the solutions were exposed to UV light for definite time periods (1 – 2 – 12 – 24 h). At each time interval, including the 30 min-dark condition, 5 ml of solution was taken and filtered by syringe filter (0.22 μm). The clear, powder-free MB supernatant solution was scanned at 200 – 800 nm range by UV-Vis spectrophotometer (Shimadzu UV-1800). The apparent degradation rate constant k (h^{-1}) was calculated by applying the Langmuir-Hinshelwood (LH) model based on first order kinetics [52]. The equation used for the calculation is shown in Eq. (3.5).

$$\ln \frac{C}{C_0} = k * t \qquad (3.5)$$

Where C is the concentration (expressed as absorbance at 664 nm, A_{664}) at time t, and C_0 is the initial concentration A_{664} at t = 0 h [52].

3.5 Biocompatibility Tests

0.05 g of each coated sample (Table 3.4) was immersed in 10 ml of SBF, for 24 h at RT, then they were filtrated and dried to obtain ZnO-PEG hybrids for investigating the biocompatibility through their SEM and FTIR analyses.

CHAPTER 4
RESULTS AND DISCUSSION ON EXPLORING THE STRUCTURE AND PHOTOCATALYTIC CAPABILITY OF ZnO NANORODS SYNTHESIZED BY CALCINATION AND SOLVOTHERMAL METHODS

In this chapter, four different ZnO morphologies were studied. Calcined samples labeled 1c and 2c (Table 3.2) and solvothermally synthesized samples labeled 3 and 4 (Table 3.3) were explored. The influence the synthesis method on the structural properties such as crystal properties, morphology, surface chemistry, and porosity were investigated. Furthermore, the band gap structure and the photocatalytic capabilities were compared. Upon concluding the chapter, a comprehensive discussion of all findings is conducted to establish an integrated view of the relationships between structure and property.

4.1 Structural Properties

The XRD results confirmed that all powder prepared in each sample could be indexed to JCPDS# 36-1451, indicating each composition resulted in the formation of pure, hexagonal ZnO (wurtzite) [53], [54], [55], [56] as shown in Figure 4.1.

The lattice parameters and crystallite sizes obtained via the Unit Cell ® software using the Debye-Scherer Formula, shown in Eq. (3.1) are presented and compared to its JCPDS card in Table 4.1. The results indicate that the lattice parameters of the ZnO crystallites remained identical and there was no significant contraction or expansion in the wurtzite lattice as a result of changes in the synthesis method or the addition of AA.

The FTIR spectra of the particles are compared in Figure 4.2. Results showed that regardless of the method used, each formulation involved the presence of the peak centered at 400 cm^{-1}, which could be assigned to stretching of Zn-O bonding [57].

Similarly, each of the formulations exhibited the C-H bonding vibration between 862 - 878 cm^{-1}. The peak centered at 1637 cm^{-1} was due to the bending vibration of the O-H group [58].

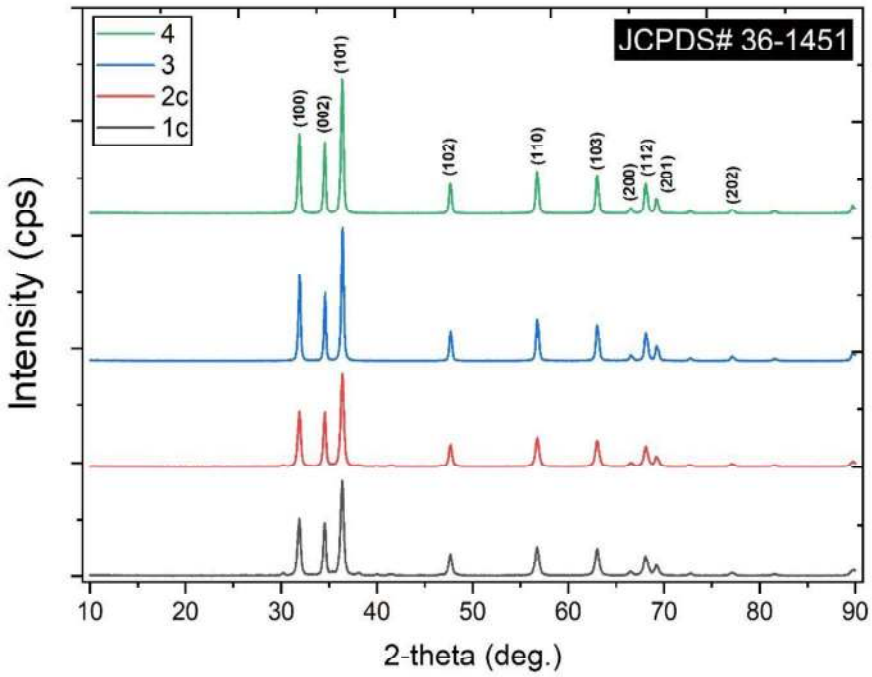

Figure 4.1. XRD patterns of ZnO nanorods

Table 4.1. Calculated lattice parameters and crystallite sizes of the ZnO crystals

Sample Code	a (Å)	c (Å)	Cell Volume ($Å^3$)	Crystallite size (nm)
1c	3.2461	5.1854	47.3191	18.83 ± 2.4
2c	3.2454	5.1905	47.3452	19.08 ± 2.4
3	3.2439	5.1859	47.2596	25.55 ± 3.36
4	3.2449	5.1941	47.3635	24.45 ± 2.5
JCPDS 36-1451	3.2480	5.2040	47.5445	20-50

The absence of this peak and the corresponding O-H bending vibration at 3415 cm^{-1} in the 1c and 2c formulations suggests that the direct calcination technique effectively eliminated the physically adsorbed water in the particles [59].

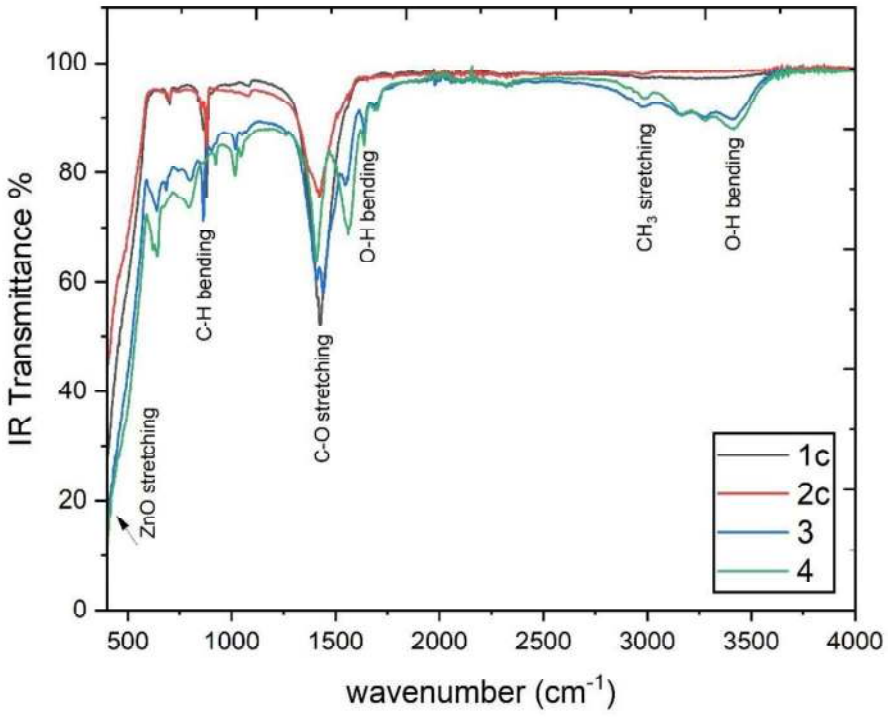

Figure 4.2. FTIR spectra of the ZnO nanorods

In order to determine if the particles possessed the same morphology and if their growth trends were influenced by the method used, SEM analysis was conducted and the resulting images are shown in Figure 4.3. The descriptions for the obtained morphologies are displayed in Table 4.2.

The images indicated that all of the samples displayed rod morphologies in nanoscale. The rods in sample 1c exhibited tendency to attach themselves on one side, making up a flower-like structure, while in sample 3, which is the solvothermally synthesized form of 1c, rods were larger in diameter. The same situation was observed between 2c and 4, but there was no remarkable morphologies change occurred due to change in synthesis method.

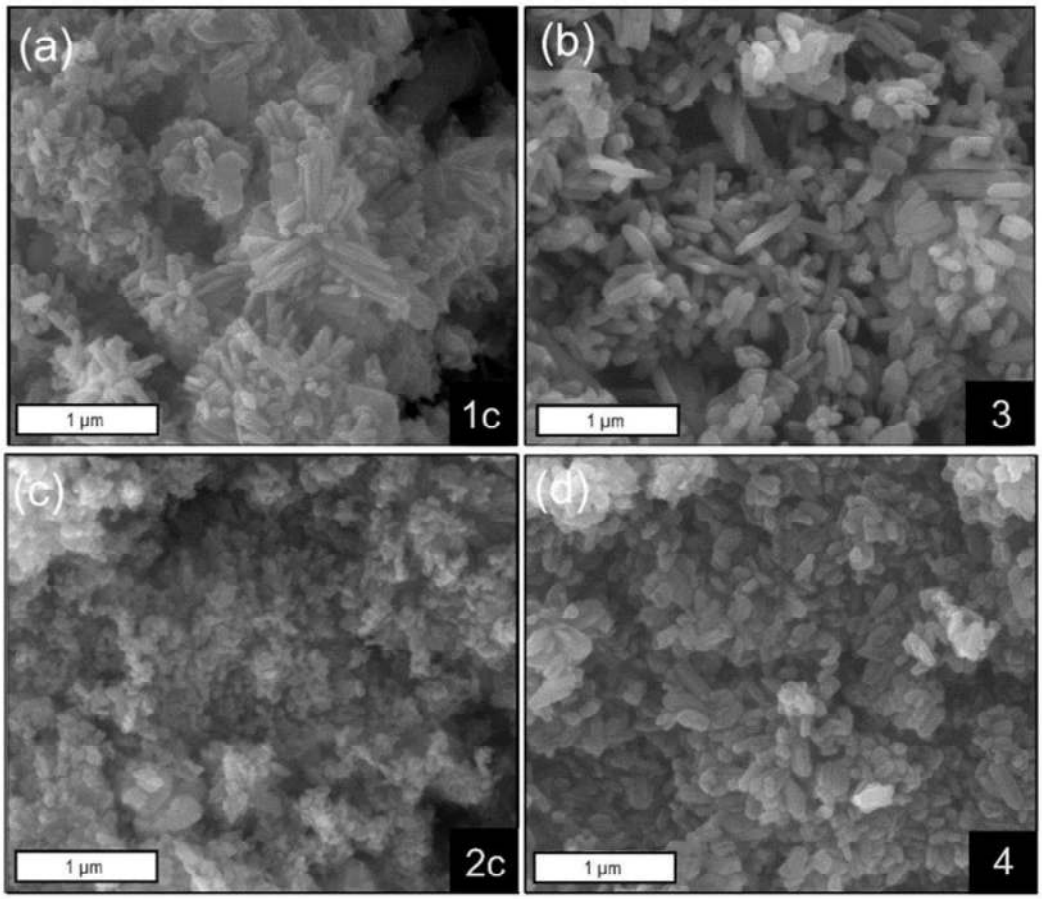

Figure 4.3. SEM images of ZnO nanorods synthesized by calcination (a, c) and solvothermal (b, d) methods

Table 4.2. The morphology descriptions of ZnO produced

Sample Code	Morphology Description
1c	Nanorods, Flower-like
2c	Nanorods
3	Nanorods with larger diameters compared to 1c
4	Nanorods with larger diameters compared to 2c

The Zn 2p and O 1s XPS spectra of the particles are displayed in Figures 4.4 and 4.5 for more-detailed comparison. The XPS spectra in Figure 4.4 revealed that the Zn 2p binding energies of the particle's surfaces exhibited significant variations. For sample 1c, the peak centered at 1020 eV was assigned to the Zn $2p_{3/2}$ binding of wurtzite structure [60], [61].

The position of the peak did not shift in sample 2c, but it was at a completely different position for the samples synthesized by solvothermal method; samples 3 (at 1019 eV) and 4 (at 1022 eV). The same condition was observed for the Zn $2p_{1/2}$ peak. It was centered at 1043 and 1044 eV for samples 1c and 2c, respectively. Whereas it shifted to 1042 eV and 1045 eV for samples 3 and 4, respectively. These results indicated that the electron density around the Zn^{2+} core of the particle surfaces was different, despite their similar morphologies [62].

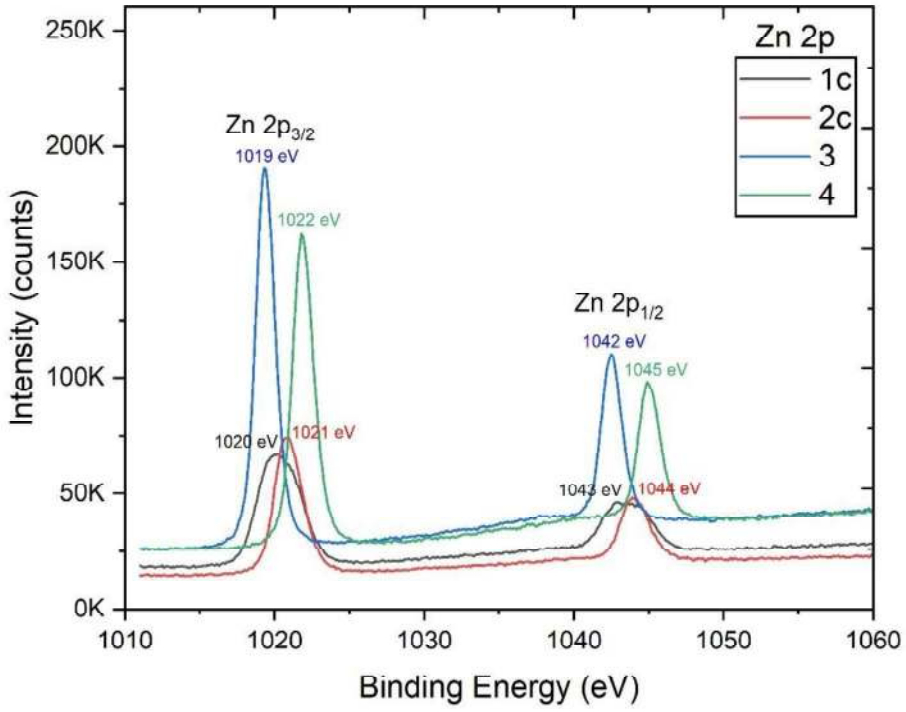

Figure 4.4. Zn 2p XPS spectra of ZnO nanorods

The O 1s binding energies indicated a similar behavior as shown in Figure 4.5 O 1s peak of samples 1c and 2c was centered at 529 eV, whereas it shifted to 527 eV and 530 eV for samples 3 and 4, respectively. The low binding energy of O 1s in calcined samples could be assigned to the O^{2-} ions in wurtzite structure. The higher binding state of sample 4 was possibly due to the oxygen deficient states on their surface [63], [64].

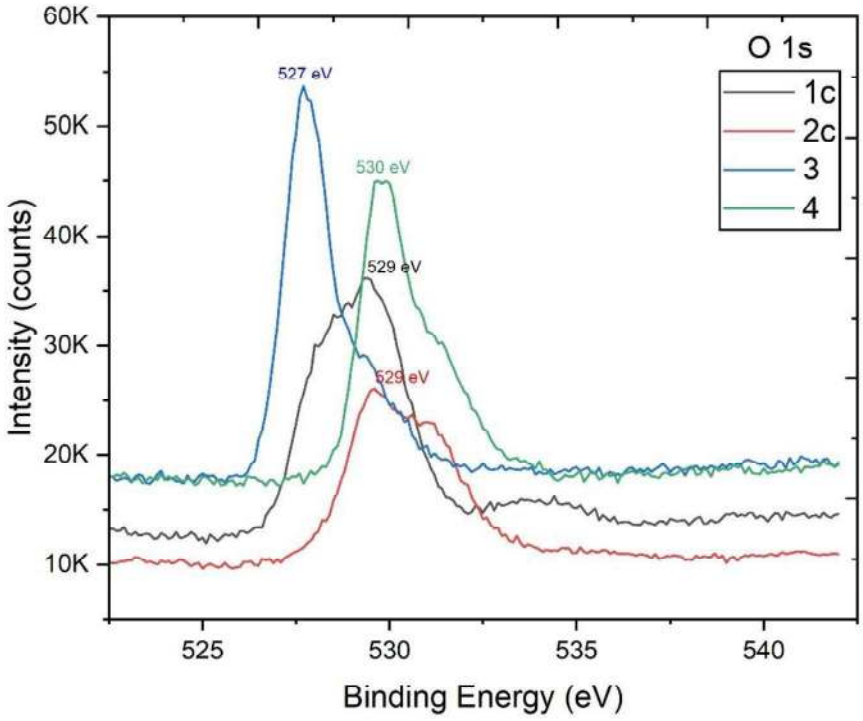

Figure 4.5. O 1s XPS spectra of ZnO nanorods

Gladys et *al.* [65] reported that the smaller binding energy shifts of surface are associated with different atomic density ({1 1 0} and {3 1 1} facets comparing with atomically rough (2 1 0) surface). Therefore, it can be stated that the surface structure is determined not only by the morphology but also by the crystalline orientation on the surface.

For physical characterization of the ZnO surfaces, Figures 4.6 and 4.7 show the gas adsorption isotherms (hysteresis) and BJH pore size distribution plots of the samples respectively. The BET isotherms shown in Figure 4.6 which indicated that the particles displayed hysteresis of type H3 according to IUPAC classification. This type of hysteresis is observed as particles have slit-shaped mesopores (2 – 50 nm) [52].

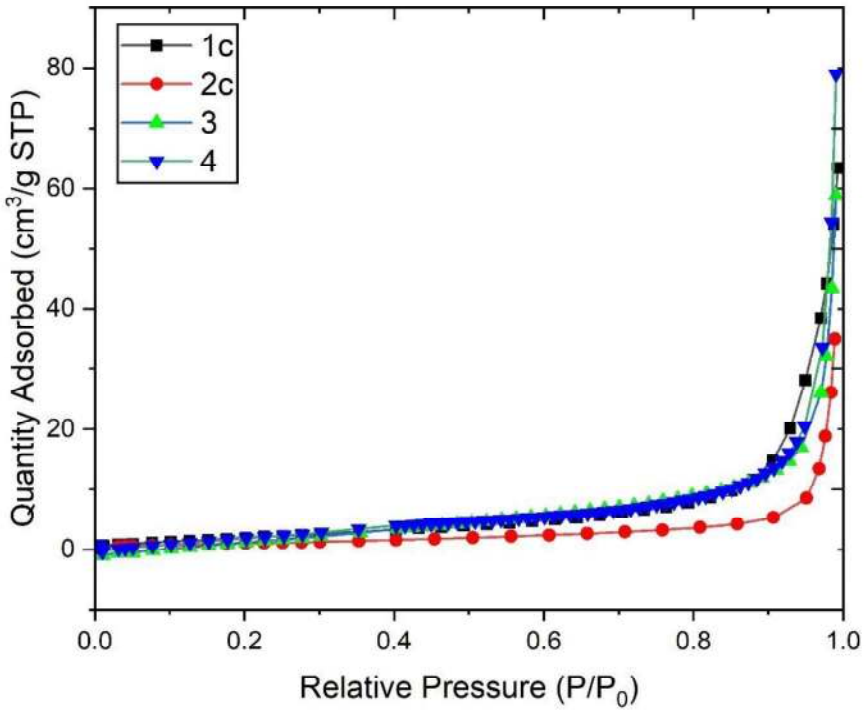

Figure 4.6. BET adsorption-desorption hysteresis of ZnO nanorods

Figure 4.7 showed that the adsorbed pore volume is higher in sample 1c, indicating a greater porosity possibly resulting from broken nanorods. The BET specific surface area (SSA), micropore surface area, and the pore widths of the samples were calculated as shown in the Table 4.3, where sample 3 has the higher SSA with lowest pore width than other samples.

Table 4.3. The gas adsorption results of ZnO particles

Sample Code	BET SSA* (m^2/g)	Micropore Surface Area (m^2/g)	Pore Width (nm)
1c	9.41212	4.40	29.2370
2c	4.5509	2.82	36.1342
3	13.0559	-	24.0539
4	10.6104	0.27	32.1071

SSA: Specific Surface Area

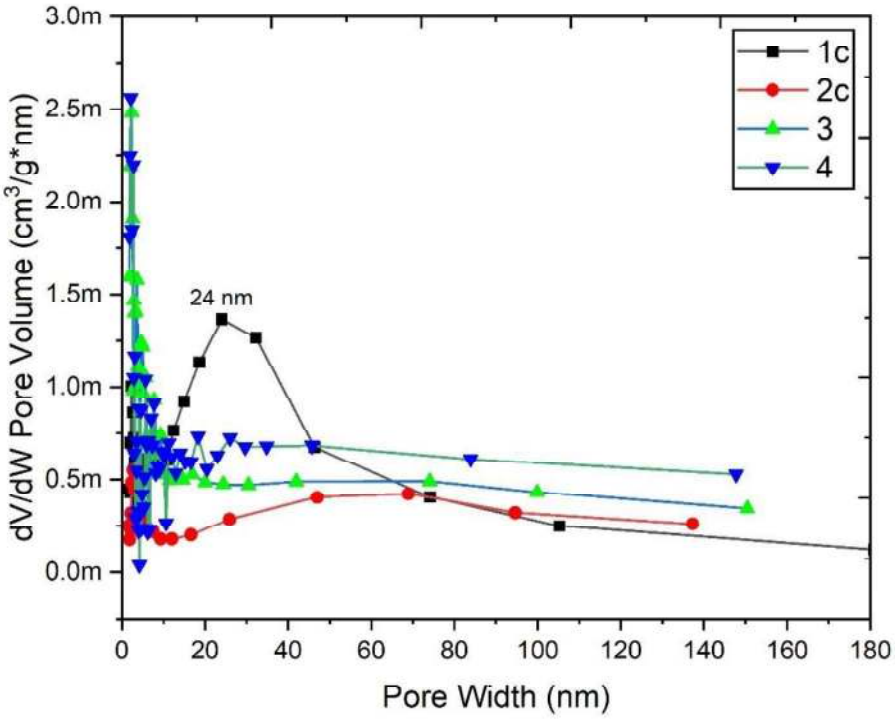

Figure 4.7. BJH pore size distribution plots of ZnO nanorods

Micropores (less than 2 nm) in ZnO particles are too small for significant photocatalytic activity, as they may not allow easy access for reactant molecules. However, they can influence the overall surface area significantly [66]. While mesopores (2 – 50 nm) are large enough to allow reactant molecules to enter and interact with the active sites but small enough to provide a high surface area, which is beneficial for photocatalytic degradation [67]. The presence of mesopores in ZnO as shown in Figure 4.7 can enhance its photocatalytic efficiency by providing more active sites and facilitating the transport of molecules [66].

4.2 Energy Band Gap and Photocatalytic Degradation Capability

In Figures 4.8 and 4.9 the optical analysis of the particles; the absorption edge and K-M transformations to obtain E_g are plotted. Figure 4.8 showed that the absorbance edge of particles was found almost identical for the samples. It was found 390 nm, 396 nm, 384 nm, and 386 nm for samples 1c, 2c, 3, and 4 respectively. The calculation was made by extrapolating the linear portion of the curve to the x-axis [68].

In Figure 4.9 and Table 4.4, The E_g values of samples are compared. The K-M transformations of each sample showed an E_g (sample 1c = 3.24 eV, sample 2c = 3.08 eV, sample 3 = 3.22 eV, and sample 4 = 3.21 eV) lower than the theoretical E_g of wurtzite ZnO (3.37 eV) [69], which means that these samples can absorb photons with lower energy, corresponding to longer wavelengths, this enhanced photocatalytic activity, i.e. in visible light range [70]. When comparing the effects of AA addition, the findings show that sample 2c, which had AA added, had a significantly smaller E_g than sample 1c. However, the E_g of the two solvothermally produced ZnO (3 and 4) did not differ from one another as Hadri et *al*. reported that the presence of AA as the stabilizing agent controls the crystal growth along planes and the optical properties does not affect, in addition to observation a slight variation of the band gap [71].

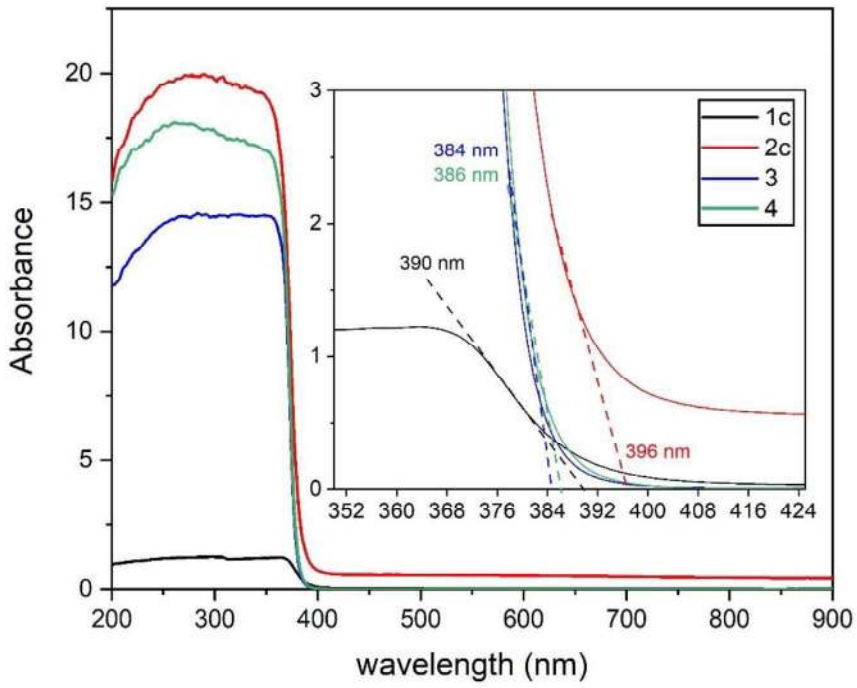

Figure 4.8. The UV-Vis absorbance of ZnO nanorods

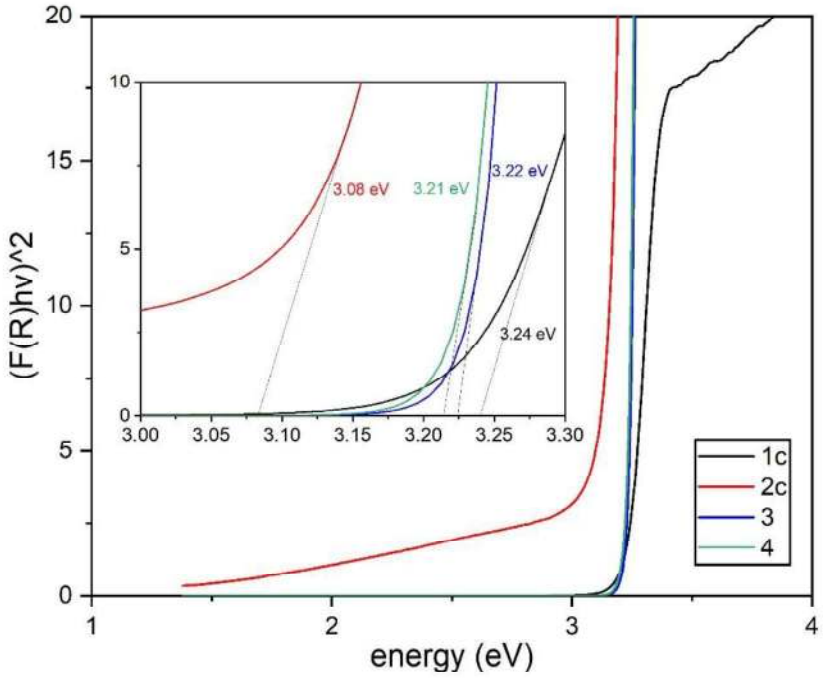

Figure 4.9. K-M transformations for the calculation of direct E_g

Table 4.4. E_g, the linear fit values, and degradation rate of ZnO particles

Sample Code	E_g (eV)	Linear Fit adj. (R^2)	kinetic rate constant K ($h^{-1} * 10^{-4}$)
1c	3.24	0.91	10 ± 2
2c	3.08	0.63	68 ± 33
3	3.22	0.92	34 ± 7
4	3.21	0.93	260 ± 21

Figures 4.10 and 4.11 present a comparison of the particles' photocatalytic degradation capability during a 24 h period. Figure 4.10 depicts the percentage of degradation over irradiation time. The initial 30 min period demonstrates the significance of the absence of UV light irradiation. Plots show that sample 3 exhibited the most significant initial degradation under dark condition (34 ± 7%). A marker of MB dye adsorption on particle surfaces was the deterioration observed in the absence of light. Samples 1c and 3 did not exhibit a significant rise in degradation % when the light was turned on, but samples 2c and 4 did, indicating that they displayed remarkable photocatalytic degradation capability. Sample 4 exhibited the greatest degradation percentage and rate in comparison to samples 1c and 2c, as predicted by prior researchers [72] who noted that solvothermal methods operating above 150 °C typically produce more active photocatalysts [73].

The degradation plots are illustrated in Figure 4.11. After 24 h of irradiation, k of sample 4 was (260 ± 21) * 10^{-4} h^{-1}, which is the highest photocatalytic kinetic rate constant and the largest surface area for interaction. As previously stated, sample 1c and sample 3 demonstrated minimal photocatalytic degradation, while sample 2c exhibited an insignificant degradation rate.

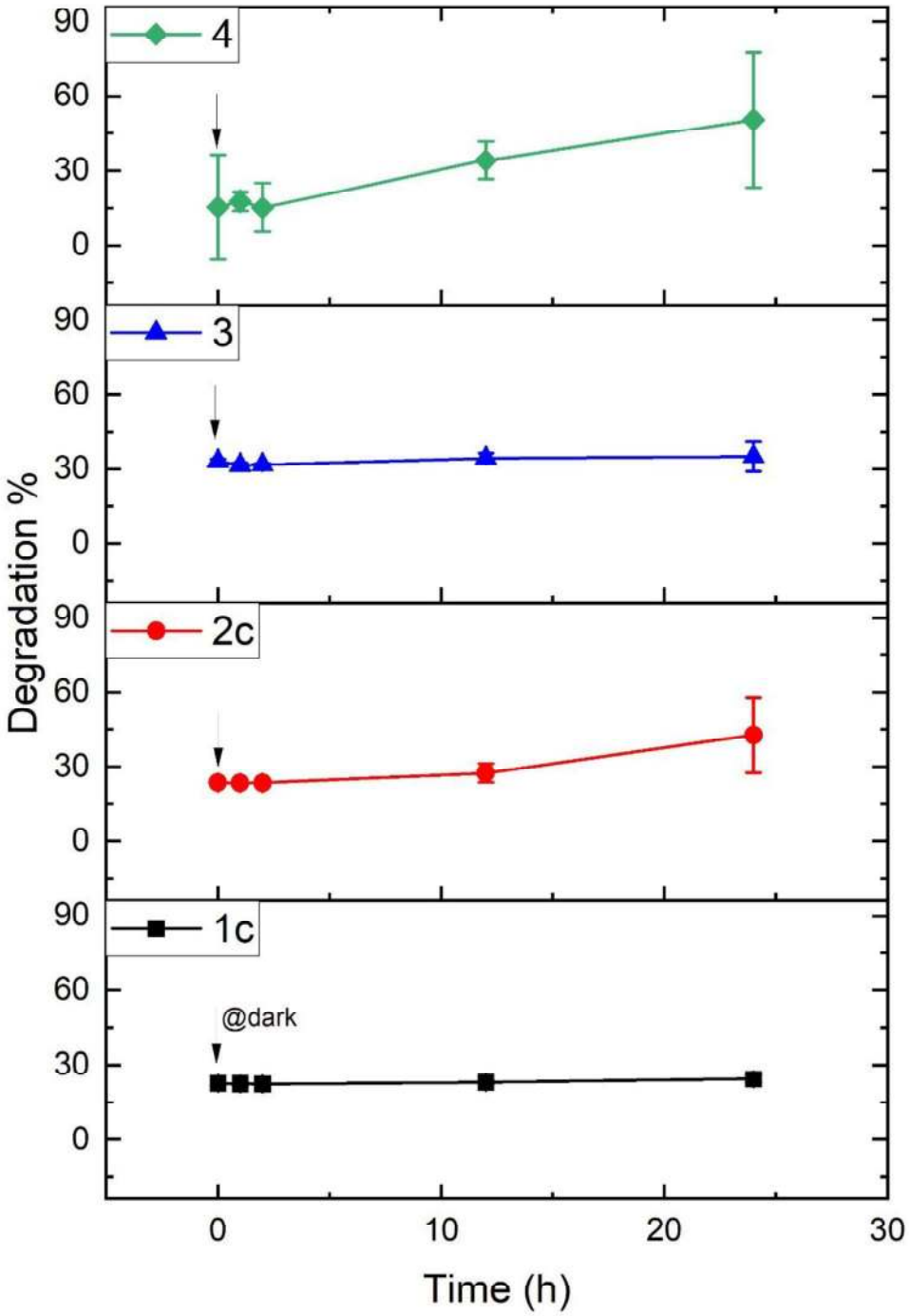

Figure 4.10. Photocatalytic degradation % of ZnO nanorods with respect to time of UV-light irradiation

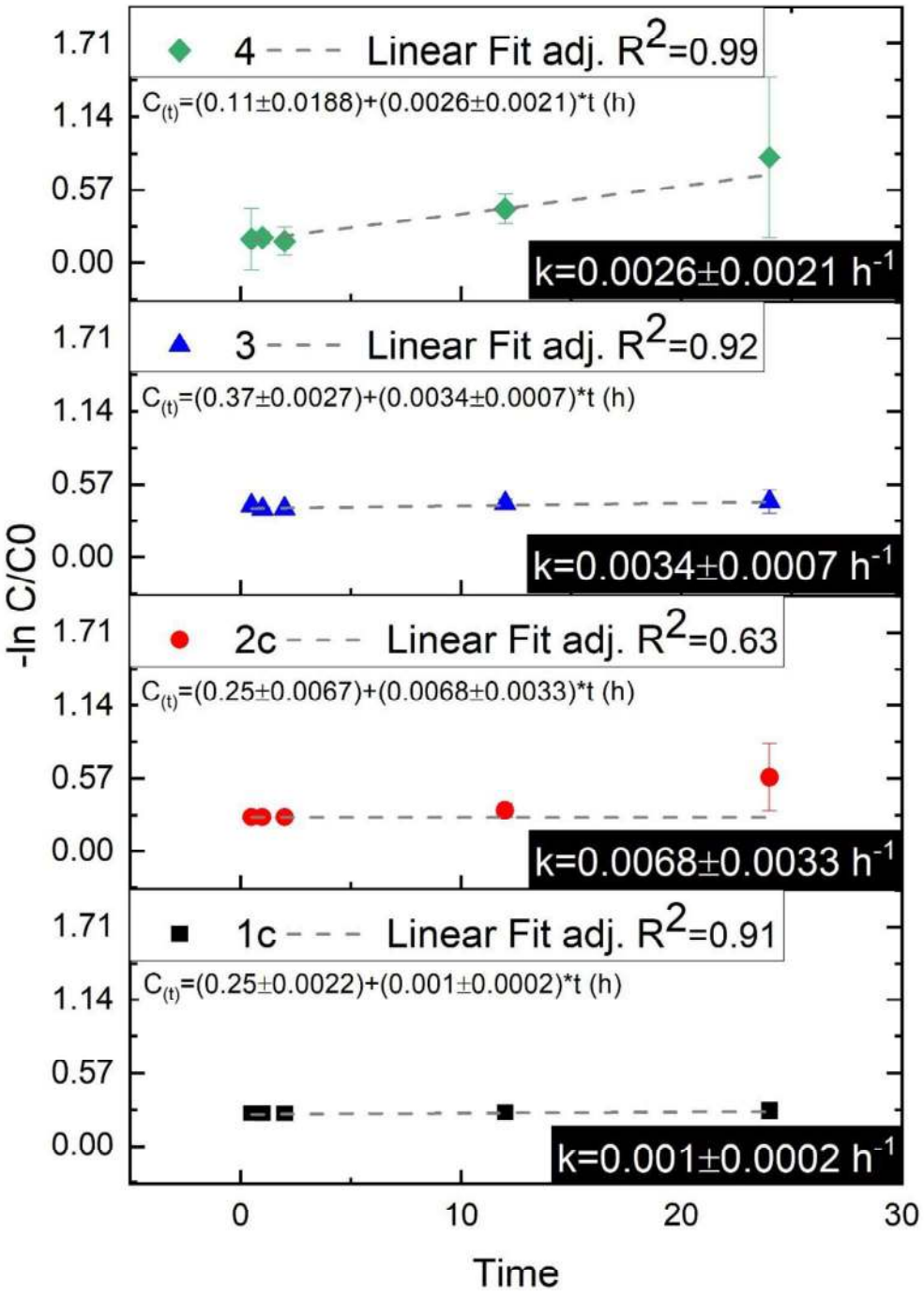

Figure 4.11. -ln C/C_0 versus UV-light irradiation time plot for the calculation of degradation rate constant (k)

4.3 Discussion on Morphological Evolution of ZnO

Four distinct morphologies of nanorods where obtained, where samples 1c and 2c were produced through the calcination technique, while samples 3 and 4 were synthesized using the solvothermal method with the identical formulation as the preceding two samples. Comparing their structures can be found in Table 4.5.

Table 4.5. Summary of structural analysis results for ZnO particles

Property/Sample code	**1c**	**2c**	**3**	**4**
Phase, crystallite size (nm)	Wurtzite, 19	Wurtzite, 19	Wurtzite, 25	Wurtzite, 24
O-H bending peak (cm^{-1})	None	None	1641, 3415	1637, 3415
Zn 2p positions (eV)	1020, 1043	1021, 1044	1019, 1042	1022, 1045
O 1s position (eV)	529	529	527	530
Morphology	Nanorods Flower-like	Nanorods	Nanorods	Nanorods
Mesopore surface area (m^2/g)	9.41	4.55	13.05	10.61
Micropore surface area (m^2/g)	4.4	2.82	-	0.27

For understanding the evolution of ZnO, it is necessary to take into account the chemical reactions that take place during the reaction. First of all, ZAD dissolves and reacts in the soluation as shown in Eq. (4.2), which is EtOH/water mixture, with/without AA (as shown in Tables 3.2 and 3.3). Then the reaction proceeds with the formation of zinc hydroxides as shown in Eq. (4.3).

$$Zn(CH_3COO)_2.2H_2O + 2C_2H_5OH \rightarrow Zn(OC_2H_5)_2 + 2CH_3COOH + H_2O \quad (4.2)$$

$$Zn(OC_2H_5)_2 + 2H_2O \rightarrow Zn(OH)_2 + 2C_2H_5OH \quad (4.3)$$

At the same time, NaOH can interact with the ZAD, by the reaction given in Eq. (4.4), then the hydroxides transform to ZnO structure by Eq. (4.5). As stated by Li et *al*. for $Zn(CH_3COO)_2$, the nucleation rate of ZnO crystallites by Eq. (4.5) depend on the concentration of OH^- ions and this concentration is controlled by the hydrolysis rate of $Zn(OC_2H_5)_2$ in Eq. (4.3) [74]. As the hydrolysis rate is increased, the crystallite size decreases. Study performed by Hadri et *al*. reported that AA addition prevent the zinc hydroxide formation, also inhibiting the electron mobility [71]. Therefore, a change in the surface chemistry and surface area are both expected for samples 2c and 4.

$$Zn(CH_3COO)_2.2H_2O + 2NaOH \rightarrow Zn(OH)_2 + 2CH_3COONa + H_2O \quad (4.4)$$

$$Zn(OH)_2 \rightarrow ZnO + H_2O \quad (4.5)$$

As shown in Table 4.1, the crystallite sizes of AA-added samples for both methods (samples 2c and 4) were larger than their AA-free samples. Therefore, it can be concluded that AA addition decreased the hydroxide content in the solution. For this reason, hydrolysis rate decreased and less amount of $Zn(OH)_2$ was obtained. This led the crystallite sizes to be larger [75]. As the electron mobility in these samples was inhibited, the Zn 2p and O 1s positions were influenced, especially during solvothermal processing.

4.4 Discussion on Photocatalytic Degradation Capability of ZnO

Except for samples 2c and 4, particles did not exhibit remarkable photocatalytic degradation capability. As illustrated in Figure 4.10, degradation on the surface of each particle varied between 15% and 34% when subjected to dark condition (for 30 min), due to the surface's susceptibility to adsorb the MB dye [76]. After UV irradiation, degradation occurred most remarkable on sample 4. For the other samples, it did not increase possibly because of recombination rate of photogenerated hole-electron pairs [77].

The O 1s spectra of samples 2c and 4 in Figure 4.5, displayed two peaks, the low and the medium binding energy components. The low one revealed the presence of O^{2-} around the Zn^{2+} core and the medium one revealed the O^{2-} defects on the surface, as mentioned by researchers that the binding energy component of the O 1s spectra can be used to compare the oxygen vacancies on the surface of the particles [78].

Using the information obtained by the XPS spectra, it can be stated that the relatively higher photocatalytic activity of samples 2c and 4 could be explained by their larger surface area (large crystallite size) and the number of O^{2-} defects.

CHAPTER 5
RESULTS AND DISCUSSION ON EXPLORING THE STRUCTURE AND PHOTOCATALYTIC CAPABILITY OF ZnO NANOSPHERES, NANOPRISMS, AND MICRO-URCHINS SOLVOTHERMALLY SYNTHESIZED AT LOW TEMPERATURE

In this chapter, three different ZnO morphologies were studied. The structure and photocatalytic capability of ZnO shown in Table 3.3 are explored. The influence of different low-temperature solvothermal procedures (100 – 200 ^{o}C) on the structural properties such as crystallinity, morphology, surface chemistry and porosity were investigated. Furthermore, the band gap structure and photocatalytic capabilities were compared. Upon concluding the chapter, a comprehensive discussion of all findings is conducted to establish an integrated view of the relationships between structure and property.

5.1 Structural Properties

The XRD patterns depicted in Figure 5.1 reveal that all of the peaks correspond to JCPDS# 36-1451, revealing that the formation of pure, hexagonal ZnO (wurtzite) was the resultant structure for each formulation [53], [54], [55], [56].

The lattice parameters and crystallite sizes obtained via the Unit Cell ® software using the Debye-Scherer Formula (Eq. 3.1) are presented and compared to its JCPDS card in Table 5.1 [79], [80], [81]. The results indicate that the lattice parameters of the ZnO crystallites remained identical and there was no significant contraction or expansion in the wurtzite lattice as a result of changes in the synthesis procedure.

XRD results revealed that the ZnO particles obtained exhibited sharp diffraction peaks, which point out that particles were formed with high crystallinity [82] and no characteristic peaks were observed other than ZnO. Considering the diffraction peak (101) which is the most intense [53], the presence of OH^- in NaOH could be a factor for formation of improved crystallinity of ZnO nanoparticles [83].

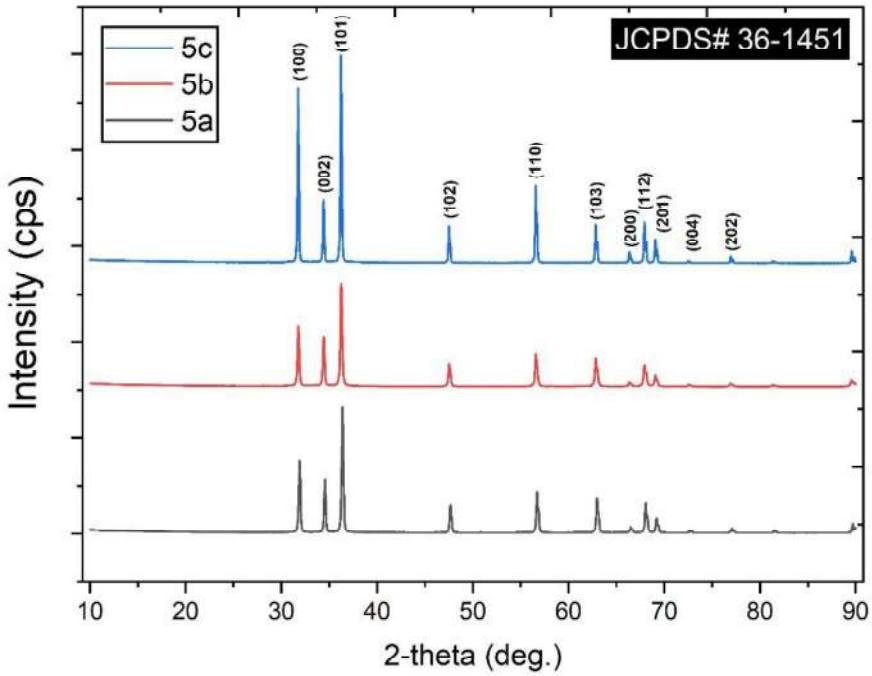

Figure 5.1. XRD patterns of ZnO morphologies solvothermally synthesized

Table 5.1. Calculated lattice parameters and crystallite sizes of the ZnO crystals

Sample Code	a (Å)	c (Å)	Cell Volume ($Å^3$)	Crystallite size (nm)
5a	3.2457	5.1965	47.4087	35 ± 4
5b	3.2573	5.2094	47.8667	32.55 ± 5
5c	3.2498	5.2080	47.6338	40.6 ± 6
JCPDS 36-1451	3.2480	5.2040	47.5445	20-50

FTIR spectra of the particles are compared in Figure 5.2 The peak centered below 400 cm^{-1} that is assigned to Zn-O bond stretching also proves the formation of ZnO structure. The other peaks were assigned to the C-H bending (863 cm^{-1}), C-O stretching (1444 cm^{-1}), O-H bending (1563 cm^{-1}) and CH_3 stretching (2976 cm^{-1}), which possibly were related to the presence of unreacted ZAD. Samples 5a and 5b lacked the O-H bending peak at around 3400 cm^{-1}, suggesting that there was no significant amount of unreacted zinc hydroxide ($Zn(OH)_2$) or physically adsorbed water on the particle surface [59]. In addition to the presence of unreacted ZAD, the micro-urchins of sample 5c showed a slight peak for Zn-OH. Results show that the ZnO precipitation reaction in the reactor was not complete during the processing of samples 5b and 5c.

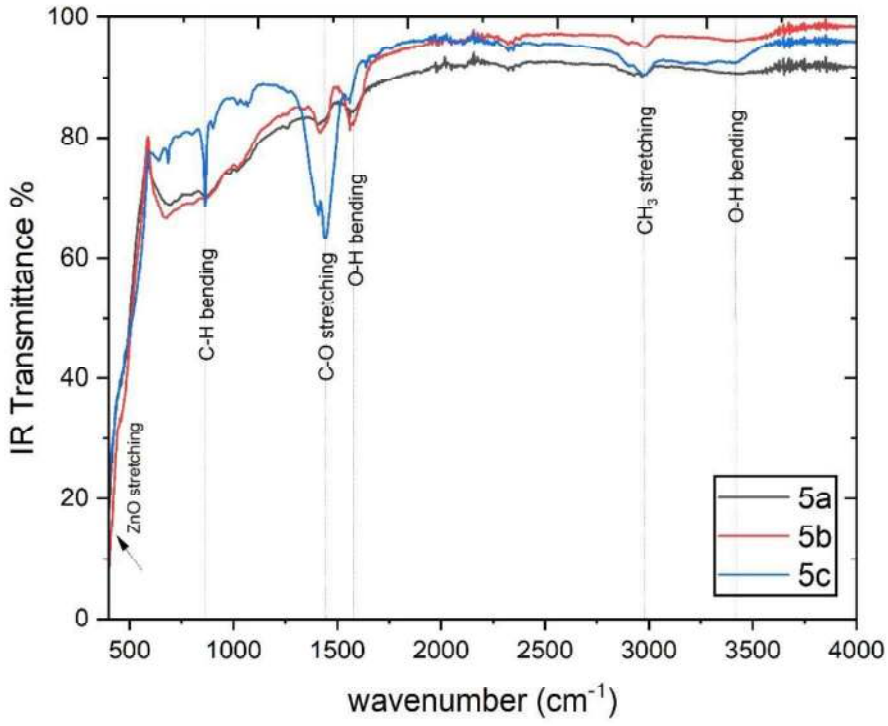

Figure 5.2. FTIR spectra of ZnO morphologies solvothermally synthesized

The growth morphologies of these particles, as determined by SEM and high-resolution TEM, are illustrated in Figure 5.3 The descriptions for the obtained morphologies are displayed in Table 5.2. Preferred growth along particular crystallographic planes was attained due to the comparatively elevated temperature, which subsequently led to the aggregation of clearly defined spherical morphologies [82]. Where at a lower temperature a different growth mechanism happened, leading to the unique triangle prismatic morphology as shown in Figure 5.3 (c, d). On the other hand, the low temperature in conjunction with the alkaline environment provided by NaOH, supported the dissolution-precipitation mechanism, fostering the growth of complex micro-urchin structures in sample 5c as shown in Figure 5.3 (e, f) [84]. Similar ZnO structures synthesized under alkaline conditions have been reported in previous studies [83], [85], [86]. TEM images Figure 5.3 (g, h, i) further substantiate the crystallinity and integrity of these diverse ZnO structures. Their growth mechanisms are discussed in Section 5.1.3, along with other analysis results.

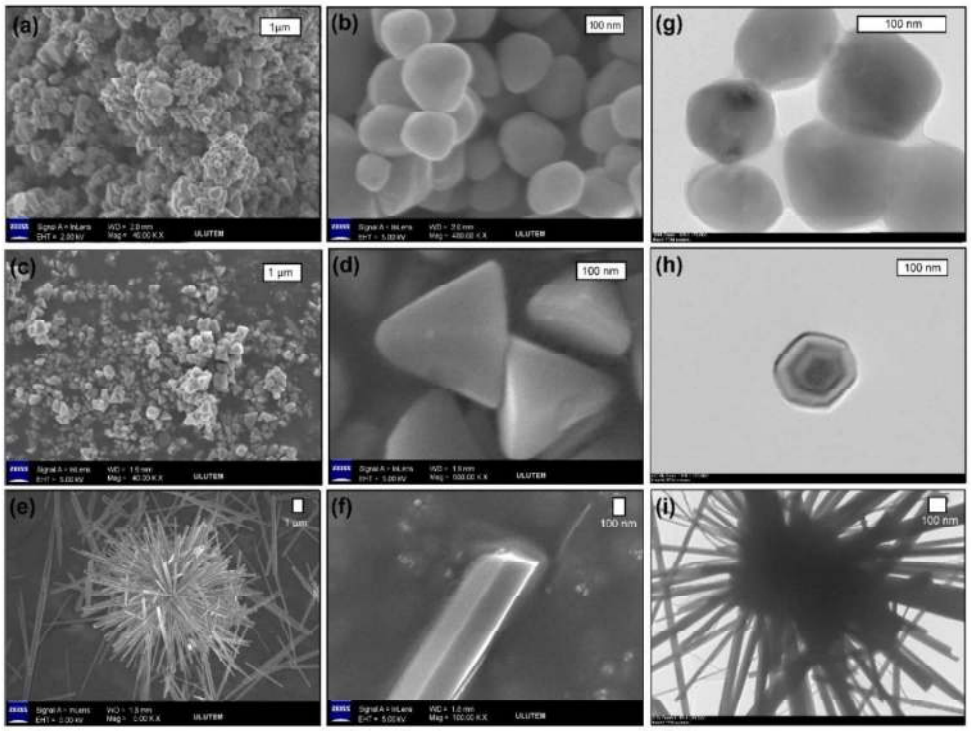

Figure 5.3. SEM images of (a, b) nanospheres "5a", (c, d) Triangular nanoprisms "5b", (e, f) Micro-urchins "5c" and TEM images of ZnO compositions grown into different morphologies g) 5a, h) 5b, i) 5c samples

Table 5.2. The morphology descriptions of ZnO particles

Sample Code	Morphology Description
5a	Nanospheres
5b	Nanoprisms
5c	Micro-urchins

The high-resolution Zn 2p and O 1s XPS spectra synthesized particles are shown in Figures 5.4 and 5.5 In the Zn 2p spectrum of sample 5a, there were two peaks centered at 1020 eV and 1042 eV, which could be assigned to the binding energies of Zn $2p_{1/2}$ and Zn $2p_{3/2}$ in wurtzite. Figure 5.4 shows that the Zn 2p binding energies of sample 5b shifted to 1022 eV and 1046 eV, respectively. For the sample 5c, Zn $2p_{3/2}$ was identical, whereas for Zn $2p_{1/2}$ it shifted to 1043 eV. These results are similar to that was observed in the work of Al-Gaashani et *al* [63]. It was disclosed that the binding energies of Zn 2p for nanorods were greater in magnitude compared to those of nanoparticles and nanoflowers.

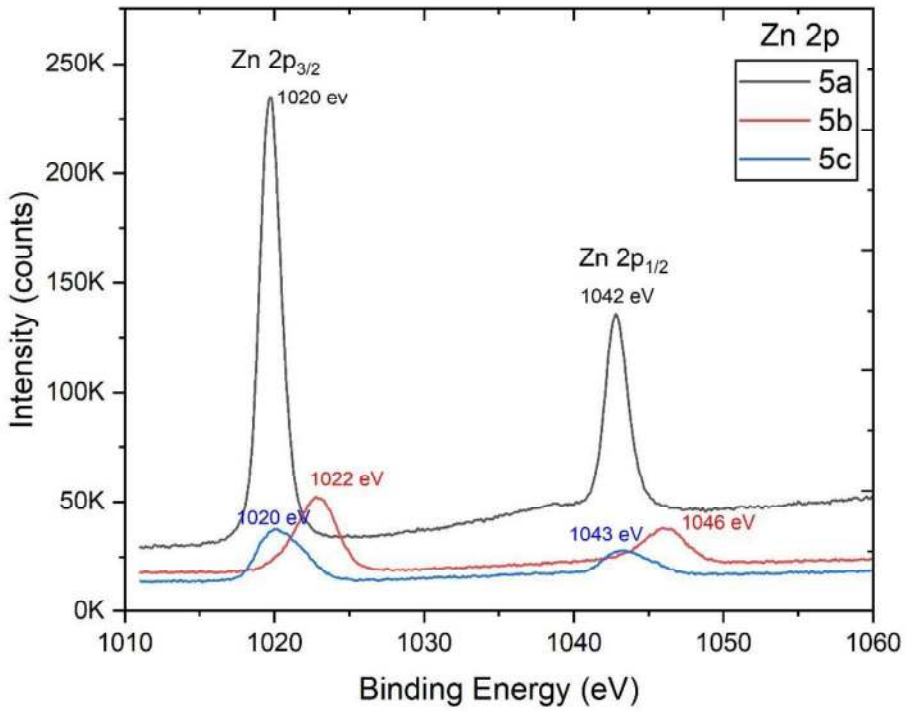

Figure 5.4. Zn 2p XPS spectra of ZnO morphologies

On the other hand, Figure 5.5 indicates that the O 1s binding energies of the ZnO particles were also different from each other. The peak was centered at 528, 532 and 530 eV for samples 5a, 5b and 5c, respectively. The low binding energy O 1s component of sample 5a at 528 eV corresponds to the O^{2-} ions in wurtzite structure. Higher binding states could be a sign of oxygen deficient states on the surface. Sample 5a nanospheres and sample 5c the micro-urchins may have possessed a greater quantity of oxygen deficiencies on their surfaces than sample 5b nanoprisms.

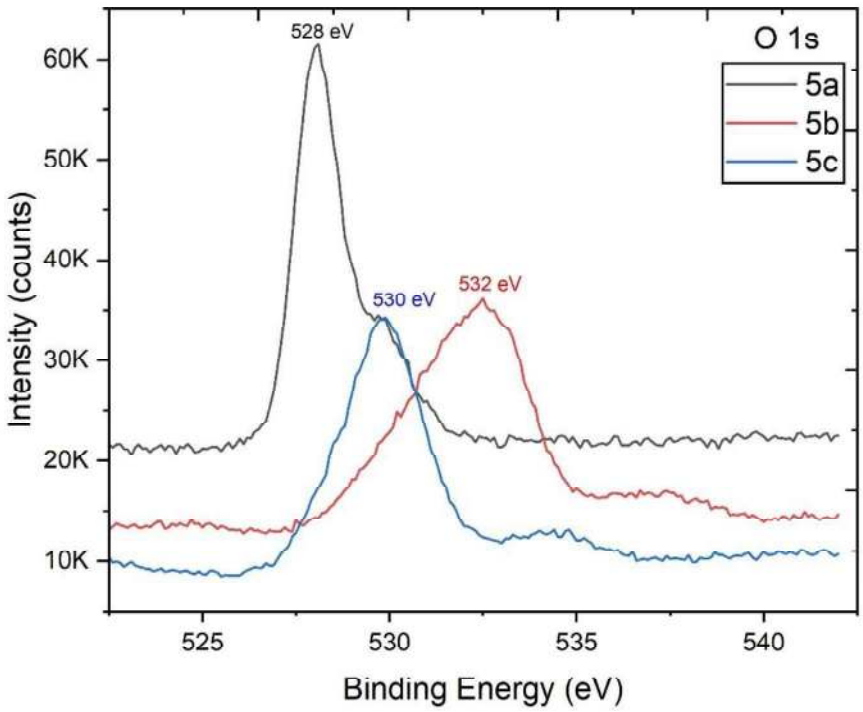

Figure 5.5. O 1s XPS spectra of ZnO morphologies

Figure 5.6 displays the Braeuer-Emmett-Teller (BET) hysteresis isotherms. The difference in the gas adsorption and desorption branches led to formation of hysteresis loops and is a sign of mesoporosity in the structure (pores of 2-50 nm). Except for sample 5b, particles indicated Type III isotherm with H3 type hysteresis which correspond to the presence of slit shaped pores between aggregates of plate-like particles. sample 5b displayed an increased volume in 0.1 - 0.3 relative pressure range; a H4 type hysteresis which was indicative of narrow slit-shaped pores [87]. On Table 5.3, the specific BET surface area and micropore area of particles are listed. As shown, sample 5b nanoprisms exhibited larger microporosity (21.66 m^2/g) than mesoporosity (15.41 m^2/g). Largest surface area was obtained by the nanospheres, then by the nanoprisms. Sample 5c micro-urchins displayed the lowest surface area. Figure 5.7 shows the distribution of pore sizes. sample 5a nanospheres exhibited peaks around 2 nm and 45 nm. Whereas sample 5b nanoprisms exhibited 25 nm average pore width. Sample 5c micro-urchins no peak, but a large pore size distribution in 20 - 160 nm.

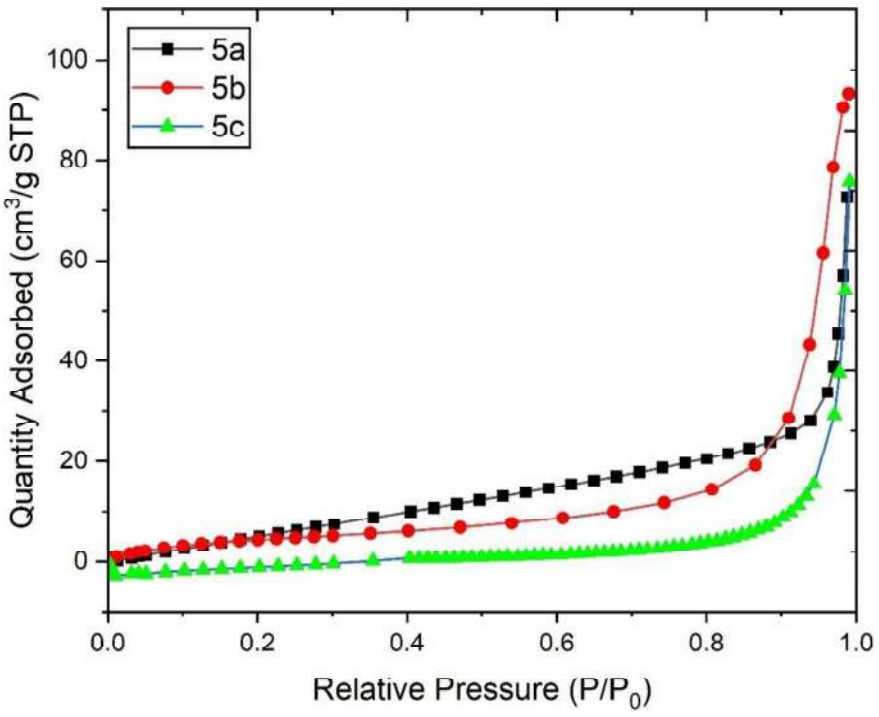

Figure 5.6. BET adsorption-desorption hysteresis of ZnO morphologies

Table 5.3. The gas adsorption results of ZnO particles

Sample Code	BET Surface Area (m^2/g)	Micropore Surface Area (m^2/g)	Pore Width (nm)
5a	30.5600	10.91	13.0095
5b	15.4158	21.66	26.7744
5c	4.4710	-	45.7488

Micropores in ZnO particles, being less than 2 nm in size, may not contribute substantially to photocatalytic activity due to their limited capacity to accommodate reactant molecules. Nevertheless, they play a crucial role in increasing the overall surface area of the particles [66]. On the other hand, mesopores, which range from 2 to 50 nm, are adequately sized to allow the entry and interaction of reactant molecules with the active sites. Their relatively small dimensions also contribute to a high surface area, which is advantageous for photocatalytic degradation [67]. As shown in Figure 5.7, the incorporation of mesopores in ZnO can significantly boost its photocatalytic efficiency. This enhancement is attributed to the increased availability of active sites and the improved transportation of molecules within the structure [66].

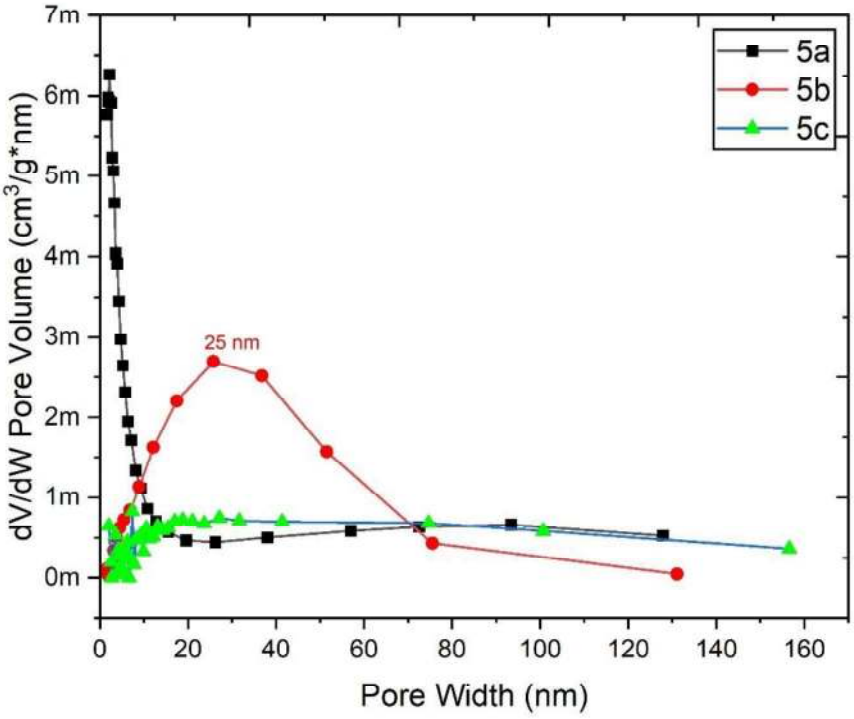

Figure 5.7. BJH pore size distribution plots of ZnO morphologies

5.2 Energy Band Gap and Photocatalytic Degradation Capability

The absorption edge and K-M transformations to obtain E_g are plotted in Figures 5.8 and 5.9 and results are listed on Table 5.4. Results indicated that the absorbance edge was found 385 nm, 387 nm, and 386 nm for samples 5a, 5b, and 5c, respectively as shown in Figure 5.8 There was no significant difference in absorbance edge of samples 5a and 5b possibly because they had identical composition and synthesis route. As shown in Figure 5.9, each sample showed an E_g (3.29 eV) slightly lower than the theoretical E_g of wurtzite ZnO (3.37 eV) [69]. The data indicated that the change in morphology from nanospheres to nanoprisms or to micro-urchins did not cause significant difference in the absorbance edge and E_g.

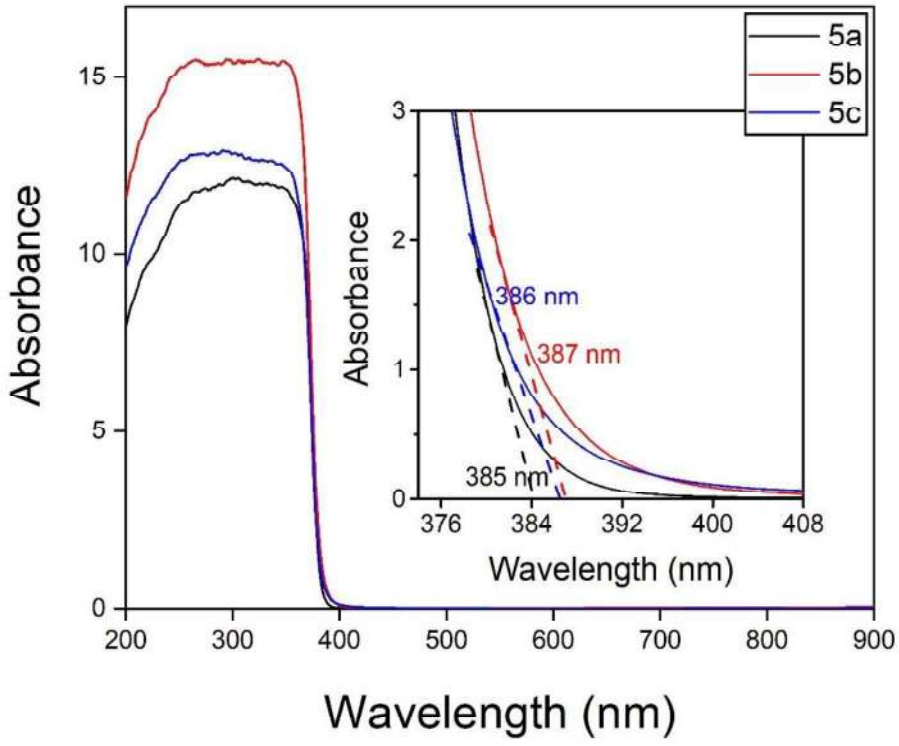

Figure 5.8. The UV-Vis absorbance plots of ZnO morphologies

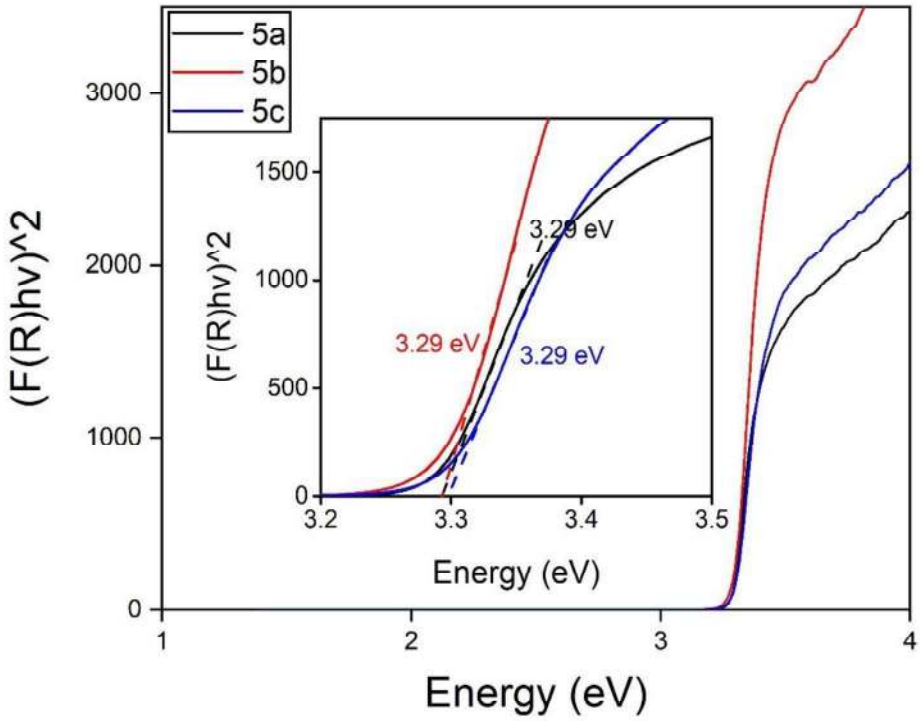

Figure 5.9. K-M transformation for direct E_g determination of ZnO morphologies

Table 5.4. E_g, the linear fit values, and degradation rate of ZnO particles

Sample Code	E_g (eV)	Linear Fit adj. (R^2)	Kinetic Rate Constant K ($h^{-1} * 10^{-4}$)
5a	3.29	0.98	26 ± 2
5b	3.29	0	-2.3 ± 2 (N/A)
5c	3.29	0.68	3.8 ± 1

Despite their similar band gap structure, the photocatalytic degradation rate of the ZnO particles was completely different. In Figures 5.10 and 5.11, the photocatalytic degradation capability of particles for 24 h are compared. Figure 5.10 shows the change in degradation % by time. The first 30 min (0.5 h) shows the value for the dark condition. For each particle type, a remarkable degradation started at dark condition and did not increase with increasing time under UV light, which indicate that surface adsorption dominated over photocatalytic degradation of MB. The degradation rate plots are showed in Figure 5.11. The degradation rate in 24 h was (26 ± 2) * 10^{-4} h^{-1} for sample 5a nanospheres, which displayed the largest surface area for interaction, was the highest. The sample 5b nanoprisms and sample 5c micro-urchins exhibited no significant photocatalytic degradation.

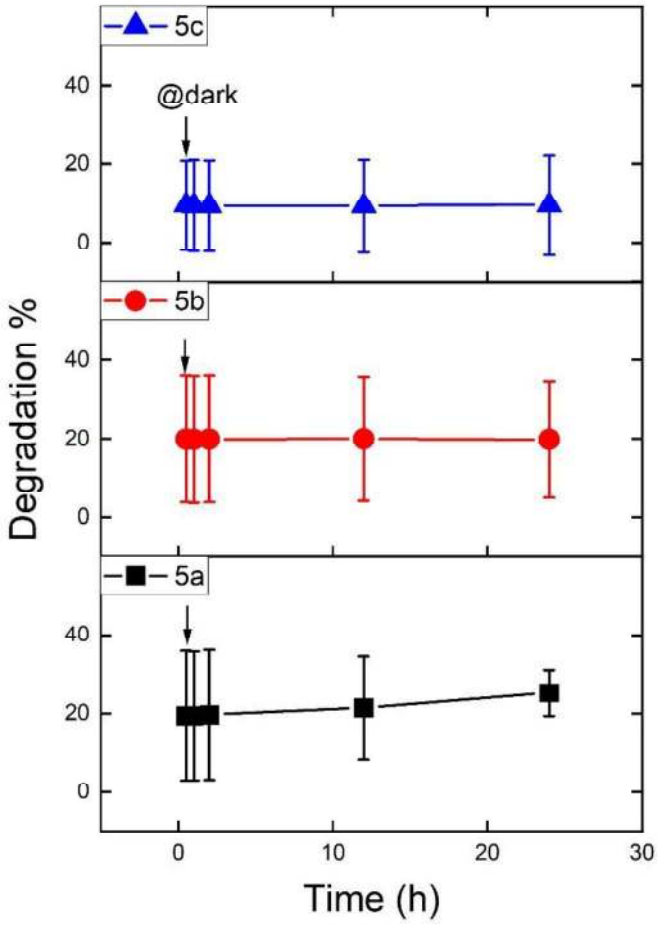

Figure 5.10. Photocatalytic degradation % of ZnO morphologies with respect to time of UV-light irradiation

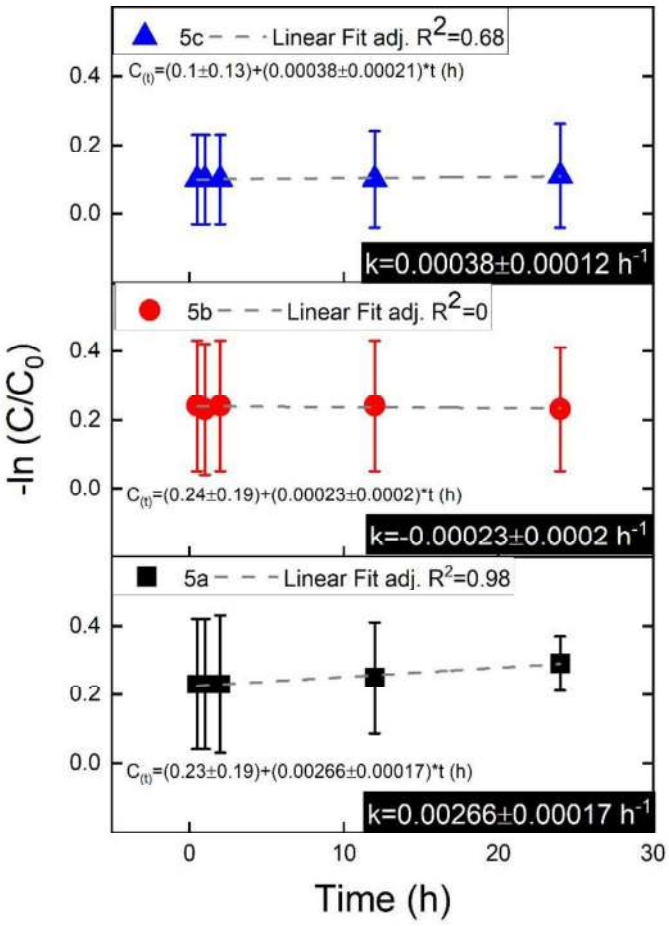

Figure 5.11. -ln C/C_0 versus UV-light irradiation time plot for the calculation of degradation rate constant (k)

5.3 Discussion on Morphological Evolution of ZnO

Three different morphologies were obtained; nanospheres (sample 5a), nanoprisms (sample 5b) and micro-urchins (sample 5c). samples 5a and 5b were formed by an identical solvothermal route in EtOH (200, 120 °C). Their structures are compared on Table 5.5.

Table 5.5. Summary of structural analysis results for ZnO particles

Property/Sample Code	**5a** **200°C, EtOH**	**5b** **120°C, EtOH**	**5c** **100°C, $NaOH_{(aq)}$**
Phase, crystallite size (nm)	Wurtzite, 35	Wurtzite, 32	Wurtzite, 40
OH bending band in FTIR spectra (cm^{-1})	None	1567	1563, 3415
Zn 2p positions (eV)	1020, 1042	1022, 1046	1020,1043
O 1s position (eV)	528, 530	532	530
Morphology	Nanosphere	Nanoprism	Micro-urchin
Mesopore surface area (m^2/g)	30.56	15.41	4.47
Micropore surface area (m^2/g)	10.91	21.66	-

The findings demonstrated that the structural characteristics of samples 5a, 5b, and 5c were comparable. Wurtzite phase with uniform crystallite size was produced. The formation of wurtzite crystals in EtOH and water can be elucidated by the reactions presented in Eq. (5.1, 5.2, 5.4) and Eq. (5.3, 5.4), respectively.

$$Zn(CH_3COO)_2.2H_2O + 2C_2H_5OH \rightarrow Zn(OC_2H5)_2 + 2CH_3COOH + H_2O \quad (5.1)$$

$$Zn(OC_2H_5)_2 + 2H_2O \rightarrow Zn(OH)_2 + 2C_2H_5OH \quad (5.2)$$

$$Zn(CH_3COO)_2.2H_2O + 2NaOH \rightarrow Zn(OH)_2 + 2CH_3COONa + H_2O \quad (5.3)$$

$$Zn(OH)_2 \rightarrow ZnO + H_2O \quad (5.4)$$

The FTIR and XPS spectra indicated the presence of a diverse chemical environment surrounding the forming atomic clusters. With the exception of the particles generated in alkaline water (sample 5c), the OH^- FTIR bands were unnoticeable. Furthermore, XPS analysis of the surfaces revealed that the Zn 2p and O 1s binding energies were different for each sample. Eq. (5.2) specifies the quantity of $Zn(OH)_2$ generated by the reaction and is associated with the OH^- bands' existence. The absence of an OH^- band in sample 5b, given that the ZAD/EtOH ratio was identical for samples 5a and 5b, can be attributed to an incomplete or gradual transformation of $Zn(OH)_2$ to ZnO, as specified by Eq. (5.3) due to decreased temperature. The observed shifts in the energy levels of the Zn $2p_{3/2}$ and $2p_{1/2}$ peaks, from 1020 to 1022 and 1042 to 1046 eV, respectively, suggest that the increased abundance of OH^- has resulted in a greater number of electrons surrounding the Zn^{2+} ions.

The O 1s peak shifted in the same manner. The low binding energy of 528 eV observed for sample 5a could be attributed to the O^{2-} ion surrounding the Zn^{2+} atom in wurtzite. Additionally, it exhibited a shoulder centered at 530 eV, which was attributed to the surface O^{2-} defects [63], [88]. The absence of these peaks and the presence of an additional peak at 532 eV in the O 1s spectrum of sample 5c indicate that there were no O^{2-} defects but rather several oxygen atoms that are loosely bonded to the surface [63]. The observed phenomenon can be attributed to the incomplete conversion of Zn $(OH)_2$ generated by Eq. (5.3) into ZnO by Eq. (5.4), a theory that is further corroborated by the OH^- bending bands seen in the FTIR spectrum of sample 5c.

Chemical variations on the surface of developing crystallites resulted in the formation of different morphologies. Despite the fact that the synthesis techniques for sample 5a and 5b were equivalent, reducing the reaction temperature resulted in a substantial shift in morphology, from nanospheres to triangular nanoprisms. Furthermore, employing

alkaline water instead of EtOH resulted in a similar outcome. Sample 5c demonstrated larger rods united on their particular surfaces resembling an urchin structure in microscale. Previous researchers conducted substantial study on the formation of ZnO crystals. They discovered that ZnO develops primarily through the Ostwald Ripening (diffusion-limited; OR) process. The addition of impurity ions such as Na^+, K^+, Li^+, might cause the growth behavior to alter into orientated attachment (OA) [89].

The spherical form of the wurtzite particles of sample 5a was in agreement with its crystal symmetry and facet surface energies, suggesting that OR was the growth process [90]. The particles were edgy nanospheres that resembled wurtzite's hexagonal structure. Because no excess OH^- was identified and the temperature and time (200°C, 24 h) were sufficient for full transformation, spherical morphology could possibly be considered as the stable form of wurtzite synthesized using this solvothermal approach with EtOH. The FTIR and XPS spectra revealed that the transition in sample 5b was incomplete, presumably because of the lower synthesis temperature (120 °C). As a result, the oxygen-deficient nanoprism morphology ought to have served as an intermediary morphology to promote the growth of edgy wurtzite spheres. This result is supported by the SEM as shown in Figure 5.12 which illustrates two morphologies present in the same powder sample. It also proves that further growth of the edgy spheres (i.e. at longer time at 200 °C) would result in the growth of nanorods (A to C transformation).

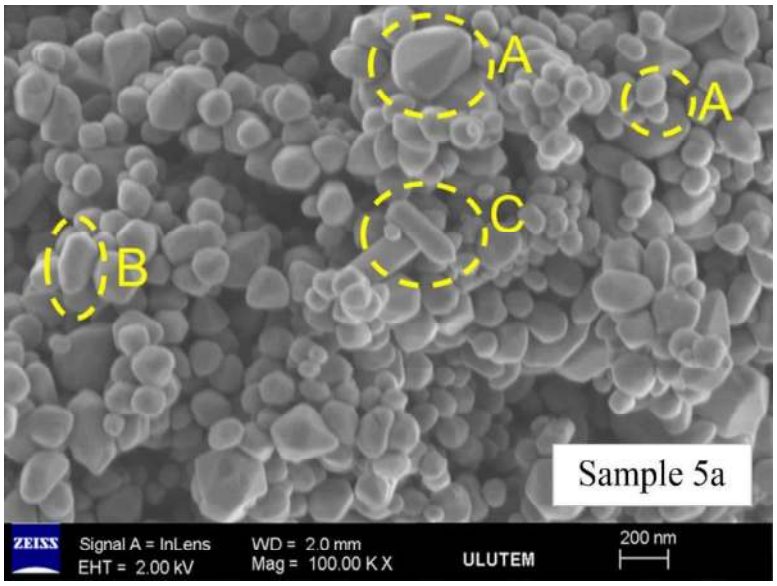

Figure 5.12. SEM image of sample 5a illustrates two morphologies

5.4 Discussion on Photocatalytic Degradation Capability of ZnO

Except for the sample 5a nanospheres, particles did not exhibit remarkable photocatalytic degradation capability. As shown in Figure 5.10, approximately 20 % of degradation occurred on the surface of each particle, under dark condition (30 min). It was because the surface of particles had high tendency to adsorb the MB dye [76]. As the UV light was on and the surfaces were irradiated with the light, degradation started most remarkably on sample 5a. The degradation did not increase under UV light, possibly due to the rate of recombination of photogenerated hole-electron pairs [77]. Previous researchers stated that the binding energy component of the O 1s spectra can be used to compare the oxygen vacancies present on the surface of particles [78]. In this manner, the O 1s spectrum of sample 5a spheres displayed two peaks, the low and the medium binding energy components at 528 and 530 eV, respectively (Figure 5.5 and Table 5.4). The low binding energy component revealed the presence of O^{2-} around the Zn^{2+} core and the medium one revealed the O^{2-} defects on the surface (The shoulder on the black curve, Figure 5.5). For the sample 5b particles, the low binding energy component was not observed but a high binding energy component at 532 eV was present, pointing out the presence of loosely bound oxygen on the surface of nanoprisms. The sample 5c particles exhibited O^{2-} defects (at 530 eV) but the surface area was low. Using the information obtained by the XPS spectra, it can be stated that the relatively higher photocatalytic activity of sample 5a could be explained by its larger surface area and the number of O^{2-} defects, as all the particles had the same E_g.

CHAPTER 6
RESULTS AND DISCUSSION ON APPLICABILITY OF ZnO NANOSTRUCTURES IN BIOMEDICAL FIELD

In this chapter, 4 types of synthesized ZnO morphologies used for the preparation of ZnO-PEG hybrid structures. The synthesized hybrids were characterized by SEM images and chemically by FTIR spectroscopy. Their biocompatibility was assessed by SBF immersion test. This work is a preliminary study to the aim of determining the potential use of this hybrids in the biomedical field.

6.1 Structure of ZnO Nanorods Hybridized with PEG

The FTIR analysis and SEM images of ZnO (2c)-PEG are shown in Figure 6.1, compared to its PEG-free counterparts.

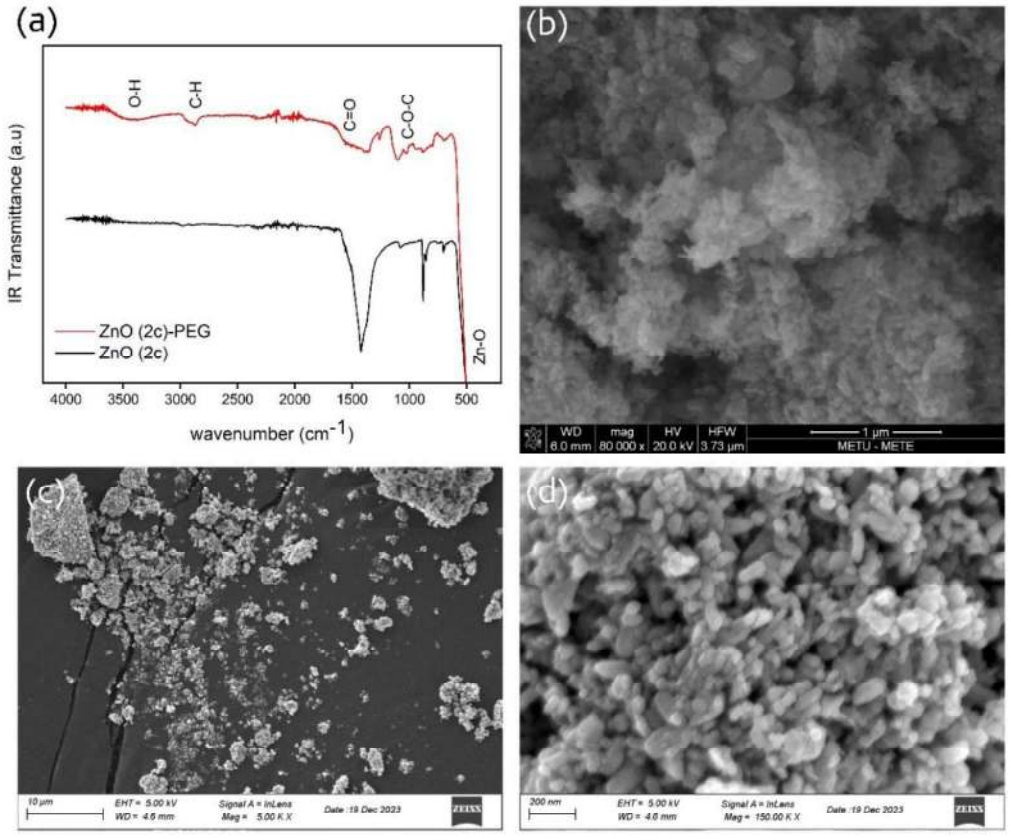

Figure 6.1. a) FTIR spectra and SEM images of b) ZnO, c) and d) ZnO (2c)-PEG

The peak at 508 cm^{-1}, assigned to the Zn-O lattice vibration, shows a decreasing in transmittance, indicating PEG's interaction with ZnO surface sites. The typical peaks associated with the carbonyl acetate groups at 1599 cm^{-1} exhibit a slight decrease after hybridization, suggesting some interaction or replacement by PEG molecules [91]. The C-O-C stretching vibrations characteristic of PEG in the 1101 cm^{-1} range also show a notable decrease in transmittance supporting the presence of PEG on the nanoparticle surface. The O-H stretch region around 3447 cm^{-1} and the C-H stretch at 2868 cm^{-1} both show a small decrease in transmittance, further confirming the attachment of PEG to the ZnO nanoparticles [45].

SEM images shows that the bare ZnO nanoparticles are rods shaped (Figure 6.1 (b)) with particle size of 20 nm consistent with XRD results, while The ZnO-PEG nanoparticles were obtained as nanorods in the same particle size as shown in Figure 6.1 (d), which confirm the little effect of the coating with the PEG as a polymer on the size and morphology of ZnO [92].

6.2 Structure of ZnO Nanoparticles Hybridized with PEG

The FTIR analysis and SEM images of ZnO (3)-PEG are shown in Figure 6.2, compared to its PEG-free counterparts.

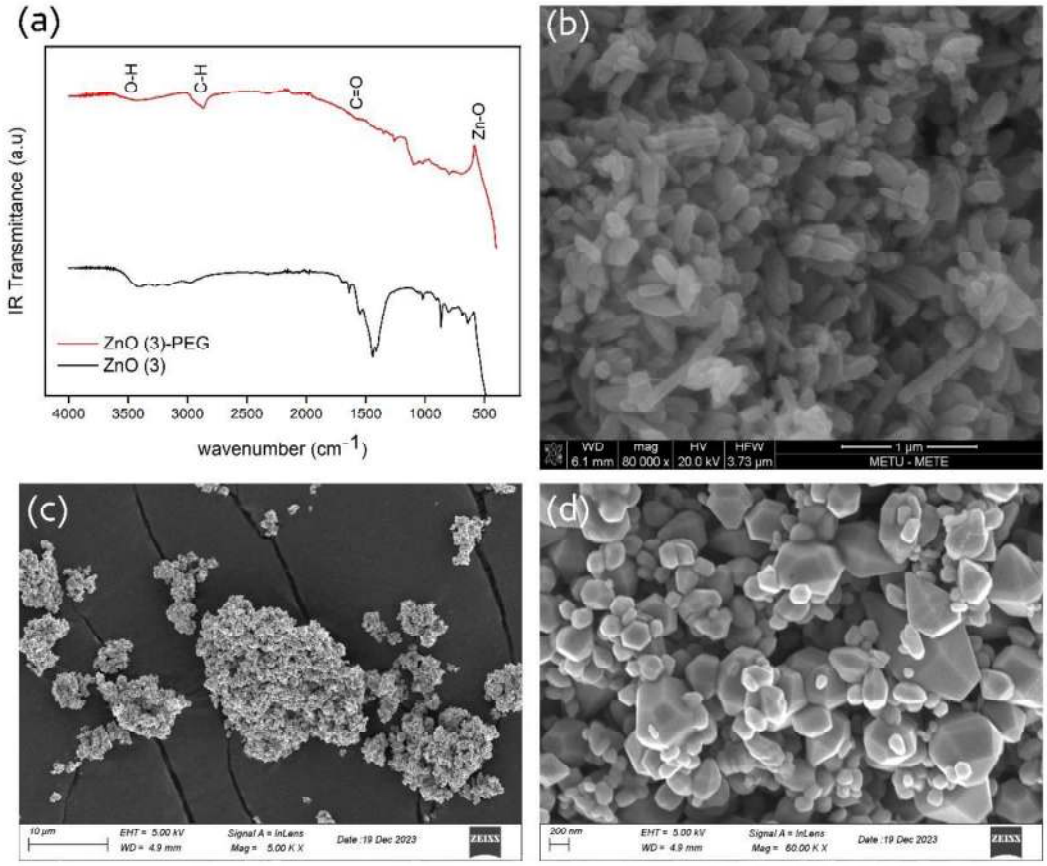

Figure 6.2. a) FTIR spectra and SEM images of b) ZnO, c) and d) ZnO (3)-PEG

The peak at 582 cm^{-1} (Zn-O bonding) decreased in transmittance, suggesting interactions between PEG molecules and the ZnO surface. The carbonyl acetate stretching vibrations, typically present in the ZnO precursor due to synthesis conditions, exhibited a transmittance decreasing at 1598 cm^{-1} after coating. This notable change indicates that PEG molecules may be replacing the surface-bound acetate groups [91]. A notable decrease in the C-O-C stretching vibration peak transmittance, at 1094 cm^{-1}, further confirms the presence of PEG on the ZnO particles surface. The O-H stretch region peak at 3499 cm^{-1} and the C-H stretch peak at 2866 cm^{-1} both show significant decreases in transmittance, reinforcing the successful hybridization [92].

SEM images shows that the bare ZnO nanoparticles are rods shaped (Figure 6.2 (b)) with particle size of 24 nm, while The ZnO-PEG nanoparticles were obtained as rods with changing shape to as like prisms with larger particle size as shown in Figure 6.2 (d), which prove the role of PEG on the size and morphology of ZnO [92].

6.3 Structure of ZnO Nanoprisms Hybridized with PEG

The FTIR analysis and SEM images of ZnO (5b)-PEG are shown in Figure 6.3, compared to its PEG-free counterparts.

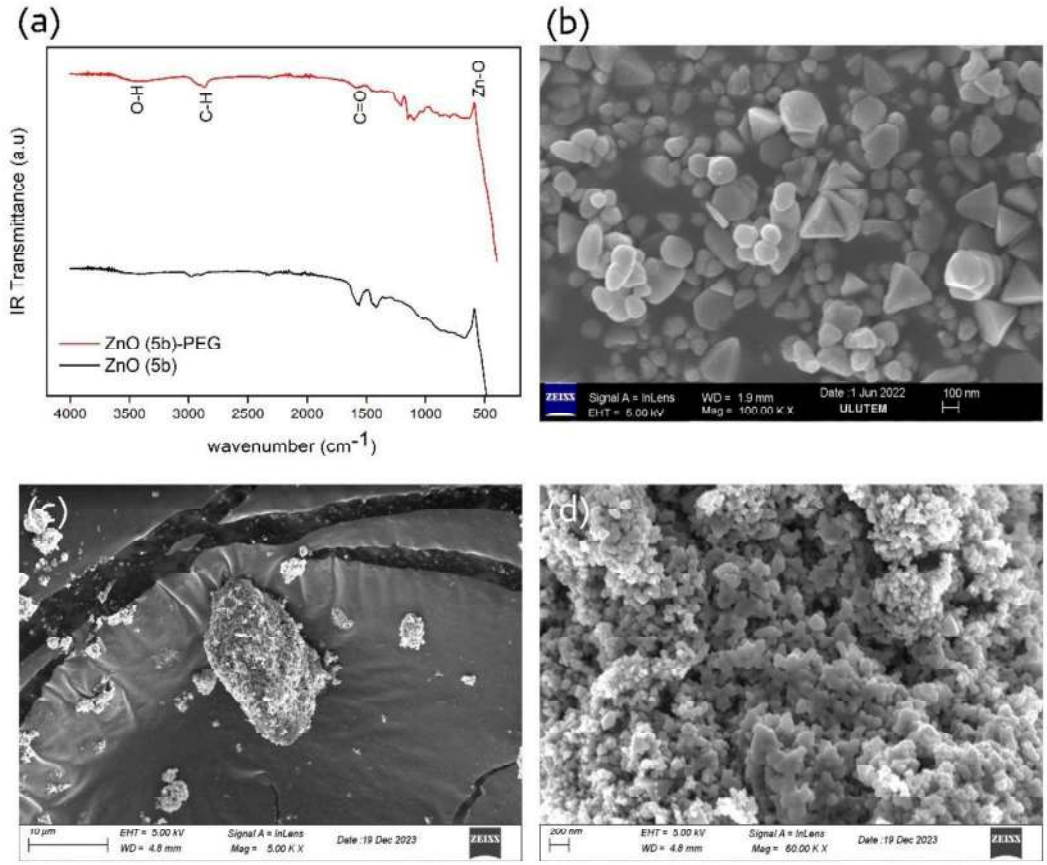

Figure 6.3. a) FTIR spectra and SEM images of b) ZnO, c) and d) ZnO (5b)-PEG

The Zn-O bond, with its characteristic peak at 588 cm^{-1}, exhibited a slight increase in transmittance, which could suggest a decreasing of surface Zn-O bonds accessible to the FTIR measurement, due to PEG surface coverage [93]. The carbonyl acetate peak at 1560 cm^{-1} shows an increase in transmittance after coating, this evidence of acetate environment modification on the ZnO surface, which may be attributed to the displacement of acetate groups by PEG molecules. The C-O-C stretching vibrations

identified at 1149 cm^{-1} decreased in transmittance, confirming the presence of PEG and suggesting strong interaction between PEG and ZnO particles surface [92]. Furthermore, the O-H stretch region at 3446 cm^{-1} and the C-H stretch at 2860 cm^{-1} both demonstrate a slight decrease in transmittance. These confirm the PEG attachment to the ZnO surface.

SEM images shows changing in the morphology after coating, changing in the particle size and shapes loosely clustered around each other was observed as shown in Figure 6.3 (d) [93].

6.4 Structure of ZnO Micro-urchins Hybridized with PEG

The FTIR analysis and SEM images of ZnO (5c)-PEG are shown in Figure 6.4, compared to its PEG-free counterparts.

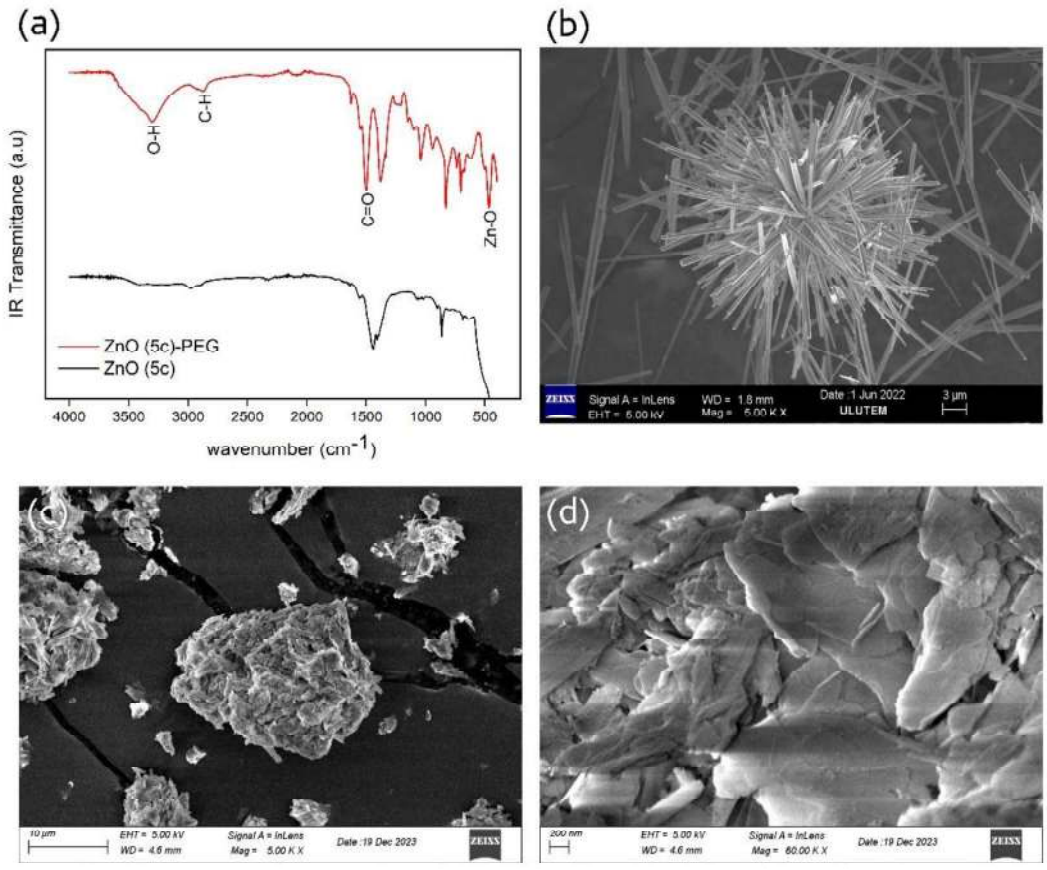

Figure 6.4. a) FTIR spectra and SEM images of b) ZnO, c) and d) ZnO (5c)-PEG

The characteristic Zn-O stretching peak at 466 cm^{-1} shows a pronounced increase in transmittance, which suggest a changing in the surface Zn-O bonds, due to PEG coating. In the carbonyl acetate region, the peak at 1497 cm^{-1} shows decreasing in transmittance after PEG coating. this large shift indicates that hybridization influences the acetate surface groups, by stopping the interaction of these groups with the IR beam or by chemical displacement [93].

The stretching of PEG, represented by the peak at 1041 cm^{-1}, also reflect a decrease in transmittance, confirming the successful coating of PEG on the ZnO surface. The O-H stretching region at 3309 cm^{-1} and the C-H stretching vibrations at 2866 cm^{-1} exhibit a decrease in transmittance, consistent with the presence of PEG.

SEM images show the urchin-shaped structures which are composed of hundreds of rods as shown in Figure 6.4 (b), while after coating with PEG, these clusters of rods were broken and formed sheet-like structure, because the instability of morphology for micro-urchins [94].

6.5 Biocompatibility of ZnO-PEG Hybrids

The SEM images of the samples coating with PEG after their immersion in SBF are shown in Figure 6.5.

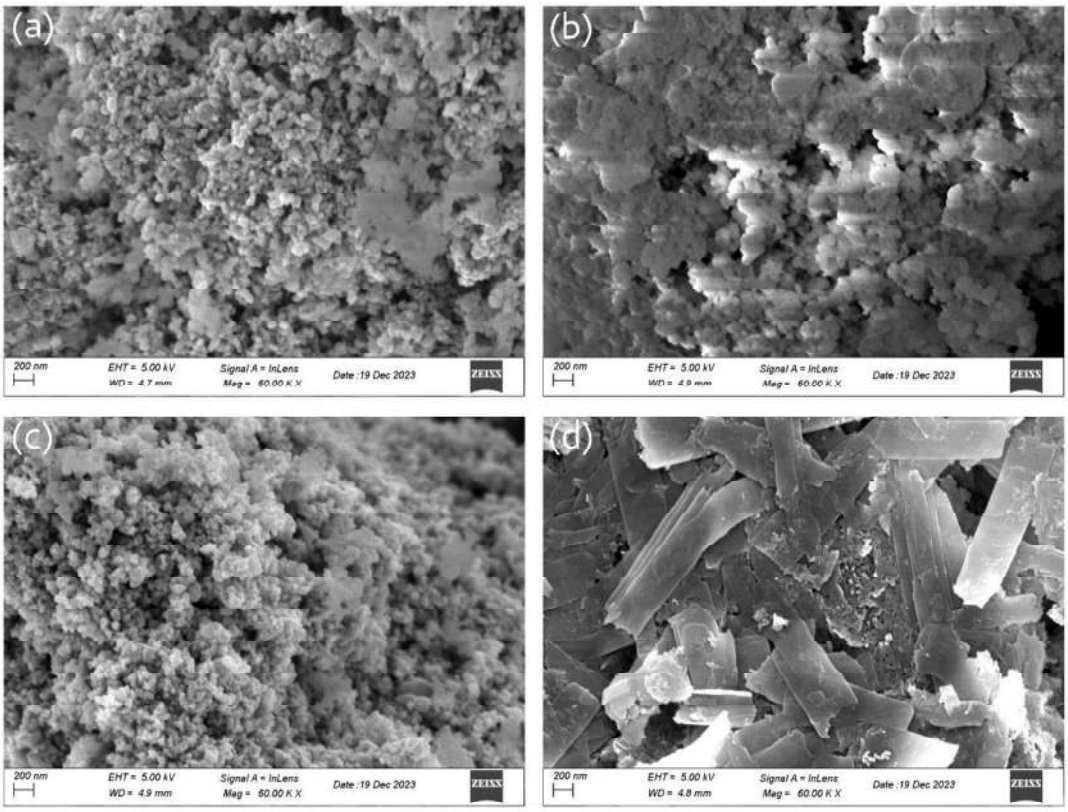

Figure 6.5. SEM images of ZnO-PEG hybrids immersed in SBF, a) sample 2c, b) sample 3, c) sample 5b, and d) sample 5c

Samples 2c and 3 before SBF immersion reveals distinct morphologies, irregular shaped particles of nanorods and big prisms-like respectively, with spreading of PEG at the ZnO surface between these nanorods and prisms. These initial morphologies are significant for understanding the initial state of the nanomaterial and its potential interaction with biological systems [95], [96]. After SBF immersion, SEM images exhibit notable changes in surface morphologies, these alterations refer to interaction between the PEG-coated ZnO surface and the SBF components, which are indicative of bioactivity and biocompatibility [97], [98]. It can be proved by hydroxyapatite (HAP, $Ca_{10}(PO_4)_6(OH)_2$) formation, where phosphate stretching bands P-O and bending mode P-O-P group should be indexed to FTIR curve of HAP [99].

For samples 5b and 5c, there are not big notable changes in the surface before and after SBF immersion, that's due to the composition of these samples (Zinc precursor and solvent only) synthesized by solvothermal or hydrothermal process at low temperatures comparing to samples 2c and 3 which contain acidic and alkaline agents synthesized at high temperatures.

CHAPTER 7
CONCLUSION AND RECOMMENDATIONS

7.1 Conclusions

In this thesis, synthesis of ZnO particles with several morphologies were studied for their use in photocatalytic and biomedical fields. The following conclusions were obtained:

- The particles synthesized had different morphologies composed in nanoscale and all the peaks of the particles synthesized were indexed to JCPDS# 36-1451, and the lattice parameters were identical to the wurtzite lattice and no characteristic peaks were observed other than ZnO.
- TEM results are in agreement with the size of particles calculated by XRD patterns, and confirmed SEM results.
- Calcination provides simplicity and cost-effectiveness but less control over particle properties, while solvothermal synthesis provides better control over size and morphology with higher costs and complexity.
- There is difference in the binding energy of Zn 2p components due to the different morphologies obtained, and the chemical valence of Zn at the surface is +2 oxidation state, because the presence of oxygen defects on the surface of ZnO particles. Each of these particles contain the presence of the peak centered at 400 cm^{-1} assigned to stretching of Zn-O bonding.
- The particles synthesized had displayed hysteresis of type H3 according to IUPAC classification, and they have slit-shaped mesopores (2 – 50 nm), but sample 5b with nanoprisms morphology had displayed hysteresis of type H4.
- The band gap energy of all samples is lower than the one of wurtzite ZnO, so these particles can absorb the photons with lower energy and longer wavelengths.
- The ZnO nanostructures demonstrated varying efficiencies in photocatalytic degradation of pollutants, attributed to differences in surface area and the presence of oxygen defects.

- The synthesis of ZnO-PEG hybrids marked a preliminary start into potential biomedical applications. These hybrids showed biocompatibility, hinting at future uses in biomedical field such as drug delivery systems.

7.2 Recommendations for Future Work

- The thesis primarily focuses on zinc acetate dihydrate and ethanol as the precursor and solvent, respectively. Future studies could explore alternative zinc precursors and solvents to synthesize ZnO nanoparticles. This could potentially lead to the discovery of new morphologies with unique photocatalytic properties.
- While the thesis explores a range of temperatures, further investigation into the effects of varying the temperature and pressure during the solvothermal synthesis could be insightful. This might lead to a deeper understanding of the relationship between synthesis conditions and the resulting ZnO structure.
- Employing more advanced characterization techniques could provide deeper insights into the nanostructure, defects, and surface properties of the ZnO nanoparticles.
- The thesis focuses on the degradation of methylene blue. Future researches could explore the photocatalytic degradation of a wider range of pollutants, including heavy metals and organic contaminants. This would expand the applicability of ZnO nanoparticles in environmental remediation.
- Combining ZnO nanoparticles with other materials (e.g., carbon nanotubes, graphene, other metal oxides) could enhance their photocatalytic efficiency.
- Expansion the synthesis process and testing the photocatalytic capabilities of ZnO nanoparticles in real-world scenarios (like wastewater treatment stations) would be a significant step toward practical applications.
- While this thesis touches on biocompatibility, further research could be directed towards specific biomedical applications of ZnO nanoparticles, such as drug delivery, and antibacterial treatments.
- Using computational tools to model the photocatalytic processes at the atomic or molecular level could offer valuable theoretical insights, complementing experimental findings.

REFERENCES

[1] V. Puspasari, A. Ridhova, A. Hermawan, M. I. Amal, and M. M. Khan, "ZnO-based antimicrobial coatings for biomedical applications," *Bioprocess and Biosystems Engineering*, vol. 45, no. 9. Springer Science and Business Media Deutschland GmbH, pp. 1421–1445, Sep. 01, 2022. doi: 10.1007/s00449-022-02733-9.

[2] G. Deshmukh, "ZnO coated nonwoven polypropylene fabric with antibacterial and antiviral function for medical applications," in *2022 International Conference on Emerging Trends in Engineering and Medical Sciences, ICETEMS 2022*, Institute of Electrical and Electronics Engineers Inc., 2022, pp. 395–400. doi: 10.1109/ICETEMS56252.2022.10093391.

[3] N. K. Shee and H.-J. Kim, "Surface Modification of ZnO with Sn(IV)-Porphyrin for Enhanced Visible Light Photocatalytic Degradation of Amaranth Dye," *Molecules*, vol. 28, no. 18, p. 6481, Sep. 2023, doi: 10.3390/molecules28186481.

[4] A. J. T. Teo, A. Mishra, I. Park, Y. J. Kim, W. T. Park, and Y. J. Yoon, "Polymeric Biomaterials for Medical Implants and Devices," *ACS Biomaterials Science and Engineering*, vol. 2, no. 4. American Chemical Society, pp. 454–472, Apr. 11, 2016. doi: 10.1021/acsbiomaterials.5b00429.

[5] Y. Wang, L. He, B. Yu, Y. Chen, Y. Shen, and H. Cong, "ZnO quantum dots modified by pH-activated charge-reversal polymer for tumor targeted drug delivery," *Polymers (Basel)*, vol. 10, no. 11, Nov. 2018, doi: 10.3390/polym10111272.

[6] S. T. Haque, M. M. Banaszak Holl, and E. H. Chowdhury, "Strategies to assemble therapeutic and imaging molecules into inorganic nanocarriers," *Frontiers of Materials Science*, vol. 16, no. 3. Higher Education Press Limited Company, Sep. 01, 2022. doi: 10.1007/s11706-022-0604-x.

[7] Z. Wang, “Functional Inorganic Nanoparticle/Polymer Hybrid Materials: Synthesis, Characterization and Self-assembly Behavior,” 2019.

[8] L. Dong and S. P. Alpay, “Role of heteroepitaxial misfit strains on the band offsets of Zn 1-xBe xO/ZnO quantum wells: A first-principles analysis,” in *Journal of Applied Physics*, Jun. 2012. doi: 10.1063/1.4729079.

[9] J. Rohrer and K. Albe, “Thermodynamic stability and electronic structure of pristine wurtzite ZnO{0001} inversion domain boundaries,” *Phys Rev Mater*, vol. 5, no. 2, Feb. 2021, doi: 10.1103/PhysRevMaterials.5.023601.

[10] A. Ashrafi and C. Jagadish, “Review of zincblende ZnO: Stability of metastable ZnO phases,” *Journal of Applied Physics*, vol. 102, no. 7. American Institute of Physics Inc., 2007. doi: 10.1063/1.2787957.

[11] D. Maouche, F. S. Saoud, and L. Louail, “Dependence of structural properties of ZnO on high pressure,” *Mater Chem Phys*, vol. 106, no. 1, pp. 11–15, Nov. 2007, doi: 10.1016/j.matchemphys.2007.05.029.

[12] O. Yanushevska, T. Dontsova, S. Nahirniak, and V. Alisova, “TiO2–ZnO Nanocomposites for Photodegradation of Dyes in Water Bodies,” in *Springer Proceedings in Physics*, Springer Science and Business Media Deutschland GmbH, 2021, pp. 719–731. doi: 10.1007/978-3-030-51905-6_49.

[13] M. Dadkhah and J. M. Tulliani, “Green Synthesis of Metal Oxides Semiconductors for Gas Sensing Applications,” *Sensors*, vol. 22, no. 13. MDPI, Jul. 01, 2022. doi: 10.3390/s22134669.

[14] S. Pal, S. Ghosh, and D. Basak, “Room temperature deposition of pulsed laser-assisted (Al, In) co-doped ZnO transparent conducting films appropriate for flexible substrates,” *Journal of Materials Science: Materials in Electronics*, vol. 32, no. 12, pp. 16682–16693, Jun. 2021, doi: 10.1007/s10854-021-06224-7.

[15] Y. Bin Eun *et al.*, “Performance Improvement of Quantum Dot Light-Emitting Diodes Using a ZnMgO Electron Transport Layer with a Core/Shell Structure,” *Materials*, vol. 16, no. 2, Jan. 2023, doi: 10.3390/ma16020600.

[16] M. Zolfaghari and M. Chireh, “Effect of Mn dopant on lattice parameters and band gap energy of semiconductor ZnO nanoparticles,” in *Advanced Materials Research*, 2014, pp. 784–789. doi: 10.4028/www.scientific.net/AMR.829.784.

[17] Ü. Özgür *et al.*, “A comprehensive review of ZnO materials and devices,” *Journal of Applied Physics*, vol. 98, no. 4. pp. 1–103, Aug. 15, 2005. doi: 10.1063/1.1992666.

[18] S.-V. Berlin and H. Gmbh, “MATERIALS SCIENCE.”

[19] J. González-Rodríguez *et al.*, “Enhanced photocatalytic activity of semiconductor nanocomposites doped with ag nanoclusters under UV and visible light,” *Catalysts*, vol. 10, no. 1, Jan. 2020, doi: 10.3390/catal10010031.

[20] F. Rahman *et al.*, “Green synthesis of ZnO nanoparticles using Cocos nucifera leaf extract: Characterization, antimicrobial, antioxidant, and photocatalytic activity”, doi: 10.1101/2022.10.27.514023.

[21] M. A. Awad, E. M. M. Ibrahim, and A. M. Ahmed, “Synthesis and thermal stability of ZnO nanowires,” *J Therm Anal Calorim*, vol. 117, no. 2, pp. 635–642, 2014, doi: 10.1007/s10973-014-3836-x.

[22] T. Mei and Y. Hu, “Synthesis, Self-assembly and Optoelectronic Properties of Monodisperse ZnO Quantum Dots.” [Online]. Available: www.intechopen.com

[23] D. Winarski and F. Selim, “Synthesis of Conductive Sol-Gel ZnO Films and Development of ZnO Printed Electronics,” in *Sol-Gel Method - Design and Synthesis of New Materials with Interesting Physical, Chemical and Biological Properties*, IntechOpen, 2019. doi: 10.5772/intechopen.82041.

[24] S. Arya *et al.*, “Review—Influence of Processing Parameters to Control Morphology and Optical Properties of Sol-Gel Synthesized ZnO Nanoparticles,” *ECS Journal of Solid State Science and Technology*, vol. 10, no. 2, p. 023002, Feb. 2021, doi: 10.1149/2162-8777/abe095.

[25] I. Ben Amor, H. Hemmami, S. E. Laouini, M. S. Mahboub, and A. Barhoum, “Sol-Gel Synthesis of ZnO Nanoparticles Using Different Chitosan Sources:

Effects on Antibacterial Activity and Photocatalytic Degradation of AZO Dye," *Catalysts*, vol. 12, no. 12, Dec. 2022, doi: 10.3390/catal12121611.

[26] A. Goudarzi, E. Zabihi, D. Shahrampour, and M. Heydari Sorshejani, "Eco-friendly synthesis of large band gap ZnO nanoparticles by trisodium citrate: investigation of annealing effect on structural and optical properties," *Journal of Materials Science: Materials in Electronics*, vol. 33, no. 29, pp. 22798–22809, Oct. 2022, doi: 10.1007/s10854-022-09047-2.

[27] "SYNTHESIS AND STRUCTURAL CHARACTERIZATION OF ZNO NANOPARTICLES", doi: 10.31891/2307-5732-2022-311-4-35-41.

[28] P. Pascariu, N. Olaru, A. Rotaru, and A. Airinei, "Innovative low-cost carbon/zno hybrid materials with enhanced photocatalytic activity towards organic pollutant dyes' removal," *Nanomaterials*, vol. 10, no. 9, pp. 1–18, Sep. 2020, doi: 10.3390/nano10091873.

[29] E. Rezaei-Aghdam, A. Shamel, M. Khodadadi-Moghaddam, G. E. Rajaei, and S. Mohajeri, "Hydrothermal synthesis of ZnO nanoparticles and comparison of its adsorption characteristics with the natural adsorbent (mango peel)," *Asian Journal of Nanoscience and Materials*, vol. 4, no. 3, pp. 188–200, Jul. 2021, doi: 10.26655/AJNANOMAT.2021.3.2.

[30] X. Zhang, L. Zhou, X. Tu, and F. Hu, "Hydrothermal synthesis of ZnO Crystals: Diverse morphologies and characterization of the photocatalytic properties," *Polyhedron*, vol. 246, Dec. 2023, doi: 10.1016/j.poly.2023.116668.

[31] K. Huszla *et al.*, "UV-light photocatalytic degradation of non-ionic surfactants using ZnO nanoparticles," *International Journal of Environmental Science and Technology*, vol. 19, no. 1, pp. 173–188, Jan. 2022, doi: 10.1007/s13762-021-03160-1.

[32] H. Lu *et al.*, "One-step electrodeposition of ZnO/graphene composites with enhanced capability for photocatalytic degradation of organic dyes," *Front Chem*, vol. 10, Nov. 2022, doi: 10.3389/fchem.2022.1061129.

[33] Z. Wang *et al.*, “Facile constructing ZnO/ZnCO3 heterojunction for high-performance photocatalytic NO oxidation and reaction pathway study,” *Journal of Materials Science: Materials in Electronics*, vol. 31, no. 6, pp. 4527–4534, Mar. 2020, doi: 10.1007/s10854-020-03002-9.

[34] L. Chen *et al.*, “ZnO nanorods/Fe 3 O 4-graphene oxide/metal-organic framework nanocomposite: recyclable and robust photocatalyst for degradation of pharmaceutical pollutants”, doi: 10.1007/s11356-020-12253-2/Published.

[35] F. H. Alkallas, A. B. G. Trabelsi, R. Nasser, S. Fernandez, J. M. Song, and H. Elhouichet, “Promising Cr-Doped ZnO Nanorods for Photocatalytic Degradation Facing Pollution,” *Applied Sciences (Switzerland)*, vol. 12, no. 1, Jan. 2022, doi: 10.3390/app12010034.

[36] A. Artesani, M. V. Dozzi, L. Toniolo, G. Valentini, and D. Comelli, “Experimental study on the link between optical emission, crystal defects and photocatalytic activity of artist pigments based on zinc oxide,” *Minerals*, vol. 10, no. 12, pp. 1–15, Dec. 2020, doi: 10.3390/min10121129.

[37] M. Hasanpour, S. Motahari, D. Jing, and M. Hatami, “Investigation of the Different Morphologies of Zinc Oxide (ZnO) in Cellulose/ZnO Hybrid Aerogel on the Photocatalytic Degradation Efficiency of Methyl Orange,” *Top Catal*, 2021, doi: 10.1007/s11244-021-01476-3.

[38] X. Ren *et al.*, “Controllable Synthesis of ZnO Nanoparticles with Improved Photocatalytic Performance for the Degradation of Rhodamine B under Ultraviolet Light Irradiation,” *Molecules*, vol. 28, no. 13, Jul. 2023, doi: 10.3390/molecules28135135.

[39] F. Opoku, K. K. Govender, C. G. C. E. Van Sittert, and P. P. Govender, “Understanding the mechanism of enhanced charge separation and visible light photocatalytic activity of modified wurtzite ZnO with nanoclusters of ZnS and graphene oxide: From a hybrid density functional study,” *New Journal of Chemistry*, vol. 41, no. 16, pp. 8140–8155, 2017, doi: 10.1039/c7nj01942d.

[40] X. Zhang *et al.*, “Carbon-Doped ZnO Nanostructures: Facile Synthesis and Visible Light Photocatalytic Applications,” *Journal of Physical Chemistry C*, vol. 119, no. 35, pp. 20544–20554, Aug. 2015, doi: 10.1021/acs.jpcc.5b07116.

[41] B. Raj, “Synergy Photodegradation of Basic Dyes by ZnO/Bi 2 O 3 Nanocomposites under Visible Light Irradiation.”

[42] M. R. J. Carroll *et al.*, “The effect of polymer coatings on proton transverse relaxivities of aqueous suspensions of magnetic nanoparticles,” *Nanotechnology*, vol. 22, no. 32, Aug. 2011, doi: 10.1088/0957-4484/22/32/325702.

[43] E. M. Múzquiz-Ramos, D. A. Cortés-Hernández, C. G. Sánchez-Torres, J. C. Escobedo-Bocardo, A. Zugasti, and X. S. Ramírez-Gómez, “Biomimetic magnetic nanoparticles for hyperthermia treatment,” in *Key Engineering Materials*, Trans Tech Publications Ltd, 2012, pp. 16–19. doi: 10.4028/www.scientific.net/KEM.493-494.16.

[44] L. Yin, Y. Pang, L. Shan, and J. Gu, “The in Vivo Pharmacokinetics of Block Copolymers Containing Polyethylene Glycol Used in Nanocarrier Drug Delivery Systems,” *Drug Metabolism and Disposition*, vol. 50, no. 6, pp. 827–836, Jun. 2022, doi: 10.1124/dmd.121.000568.

[45] B. Raisi Dehkourdi, S. Fatahian, and K. Shahanipoor, “Synthesis, Characterization and renal toxicity of ZnO and polyethylene glycol Coated ZnO nanoparticles,” vol. 4, no. 1, pp. 55–60, 2017, doi: 10.22038/nmj.2017.8054.

[46] S. Abbasi, M. R. Bilesan, and F. Golestani-Fard, “In vitro evaluation of the biocompatibility and bioactivity of plasma electrolyte oxidized titania/calcium phosphate nanocoatings on Ti,” *J Mater Sci*, vol. 54, no. 5, pp. 4277–4286, Mar. 2019, doi: 10.1007/s10853-018-3147-x.

[47] J. Buczynska, E. Pamula, and S. Blazewicz, “Mechanical properties of (poly(L-lactide-co-glycolide))-based fibers coated with hydroxyapatite layer,” *J Appl Polym Sci*, vol. 121, no. 6, pp. 3702–3709, Sep. 2011, doi: 10.1002/app.34189.

[48] T. Kokubo and H. Takadama, “How useful is SBF in predicting in vivo bone bioactivity?,” *Biomaterials*, vol. 27, no. 15, pp. 2907–2915, 2006, doi: 10.1016/j.biomaterials.2006.01.017.

[49] S. Rani, P. Suri, P. K. Shishodia, and R. M. Mehra, “Synthesis of nanocrystalline ZnO powder via sol-gel route for dye-sensitized solar cells,” *Solar Energy Materials and Solar Cells*, vol. 92, no. 12, pp. 1639–1645, 2008, doi: 10.1016/j.solmat.2008.07.015.

[50] S. Mustapha *et al.*, “Comparative study of crystallite size using Williamson-Hall and Debye-Scherrer plots for ZnO nanoparticles,” *Advances in Natural Sciences: Nanoscience and Nanotechnology*, vol. 10, no. 4, 2019, doi: 10.1088/2043-6254/ab52f7.

[51] P. Makuła, M. Pacia, and W. Macyk, “How To Correctly Determine the Band Gap Energy of Modified Semiconductor Photocatalysts Based on UV-Vis Spectra,” *Journal of Physical Chemistry Letters*, vol. 9, no. 23. American Chemical Society, pp. 6814–6817, Dec. 06, 2018. doi: 10.1021/acs.jpclett.8b02892.

[52] D. Kapusuz Yavuz, “Template-free hierarchical TiO2 synthesis: Investigations of structural, optical, and photocatalytic property relationships,” *J Photochem Photobiol A Chem*, vol. 444, Oct. 2023, doi: 10.1016/j.jphotochem.2023.114888.

[53] M. J. Haque, M. M. Bellah, M. R. Hassan, and S. Rahman, “Synthesis of ZnO nanoparticles by two different methods & comparison of their structural, antibacterial, photocatalytic and optical properties,” *Nano Express*, vol. 1, no. 1, Jun. 2020, doi: 10.1088/2632-959X/ab7a43.

[54] S. Dutta, S. Chattopadhyay, A. Sarkar, M. Chakrabarti, D. Sanyal, and D. Jana, “Role of defects in tailoring structural, electrical and optical properties of ZnO,” *Progress in Materials Science*, vol. 54, no. 1. pp. 89–136, Jan. 2009. doi: 10.1016/j.pmatsci.2008.07.002.

[55] S. Senthilkumaar, K. Rajendran, S. Banerjee, T. K. Chini, and V. Sengodan, “Influence of Mn doping on the microstructure and optical property of ZnO,”

Mater Sci Semicond Process, vol. 11, no. 1, pp. 6–12, Feb. 2008, doi: 10.1016/j.mssp.2008.04.005.

[56] O. Lupan *et al.*, "Synthesis and characterization of ZnO nanowires for nanosensor applications," *Mater Res Bull*, vol. 45, no. 8, pp. 1026–1032, Aug. 2010, doi: 10.1016/j.materresbull.2010.03.027.

[57] M. Gharagozlou and S. Naghibi, "Sensitization of ZnO nanoparticle by vitamin B12: Investigation of microstructure, FTIR and optical properties," *Mater Res Bull*, vol. 84, pp. 71–78, Dec. 2016, doi: 10.1016/j.materresbull.2016.07.029.

[58] S. Jurablu, M. Farahmandjou, and T. P. Firoozabadi, "Sol-Gel Synthesis of Zinc Oxide (ZnO) Nanoparticles: Study of Structural and Optical Properties," *Journal of Sciences, Islamic Republic of Iran*, vol. 26, no. 3, pp. 281–285, 2015, [Online]. Available: http://jsciences.ut.ac.ir

[59] Y. Khan, S. K. Durrani, M. Mehmood, J. Ahmad, M. R. Khan, and S. Firdous, "Low temperature synthesis of fluorescent ZnO nanoparticles," *Appl Surf Sci*, vol. 257, no. 5, pp. 1756–1761, Dec. 2010, doi: 10.1016/j.apsusc.2010.09.011.

[60] P. S. Vindhya, S. Suresh, R. Kunjikannan, and V. T. Kavitha, "Antimicrobial, antioxidant, cytotoxicity and photocatalytic performance of Co doped ZnO nanoparticles biosynthesized using Annona Muricata leaf extract," *J Environ Health Sci Eng*, vol. 21, no. 1, pp. 167–185, Jun. 2023, doi: 10.1007/s40201-023-00851-4.

[61] I. Ahmad *et al.*, "Rare earth co-doped ZnO photocatalysts: Solution combustion synthesis and environmental applications," *Sep Purif Technol*, vol. 237, Apr. 2020, doi: 10.1016/j.seppur.2019.116328.

[62] S. Bram *et al.*, "Zn2+ Ion Surface Enrichment in Doped Iron Oxide Nanoparticles Leads to Charge Carrier Density Enhancement," *ACS Omega*, vol. 3, no. 11, pp. 16328–16337, Nov. 2018, doi: 10.1021/acsomega.8b02411.

[63] R. Al-Gaashani, S. Radiman, A. R. Daud, N. Tabet, and Y. Al-Douri, "XPS and optical studies of different morphologies of ZnO nanostructures prepared by

microwave methods," *Ceram Int*, vol. 39, no. 3, pp. 2283–2292, Apr. 2013, doi: 10.1016/j.ceramint.2012.08.075.

[64] J. Das *et al.*, "Micro-Raman and XPS studies of pure ZnO ceramics," *Physica B Condens Matter*, vol. 405, no. 10, pp. 2492–2497, May 2010, doi: 10.1016/j.physb.2010.03.020.

[65] M. J. Gladys, I. Ermanoski, G. Jackson, J. S. Quinton, J. E. Rowe, and T. E. Madey, "A high resolution photoemission study of surface core-level shifts in clean and oxygen-covered Ir(2 1 0) surfaces," *J Electron Spectros Relat Phenomena*, vol. 135, no. 2–3, pp. 105–112, Apr. 2004, doi: 10.1016/j.elspec.2004.02.109.

[66] A. E. A. E. Albadri, M. A. Ben Aissa, A. Modwi, and S. M. Saleh, "Synthesis of Mesoporous Ru-ZnO@g-C3N4 Nanoparticles and Their Photocatalytic Activity for Methylene Blue Degradation," *Water (Switzerland)*, vol. 15, no. 3, Feb. 2023, doi: 10.3390/w15030481.

[67] "Purba 2023 - enhanced photocatalytic of ZnO".

[68] A. Chandran, N. Francis, T. Jose, and K. C. George, "SYNTHESIS, STRUCTURAL CHARACTERIZATION AND OPTICAL BANDGAP DETERMINATION OF ZNS NANOPARTICLES."

[69] C. F. Klingshirn, "ZnO: Material, physics and applications," *ChemPhysChem*, vol. 8, no. 6. Wiley-VCH Verlag, pp. 782–803, Apr. 23, 2007. doi: 10.1002/cphc.200700002.

[70] A. Di Mauro, M. E. Fragalà, V. Privitera, and G. Impellizzeri, "ZnO for application in photocatalysis: From thin films to nanostructures," *Materials Science in Semiconductor Processing*, vol. 69. Elsevier Ltd, pp. 44–51, Oct. 01, 2017. doi: 10.1016/j.mssp.2017.03.029.

[71] A. Hadri, C. Nassiri, F. Z. Chafi, M. Loghmarti, and A. Mzerd, "Effect of Acetic Acid Adding on Structural, Optical and Electrical Properties of Sprayed ZnO Thin Films," *Energy and Environment Focus*, vol. 4, no. 1, pp. 12–17, Mar. 2015, doi: 10.1166/eef.2015.1129.

[72] F. Lu, W. Cai, and Y. Zhang, “ZnO hierarchical micro/nanoarchitectures: Solvothermal synthesis and structurally enhanced photocatalytic performance,” *Adv Funct Mater*, vol. 18, no. 7, pp. 1047–1056, Apr. 2008, doi: 10.1002/adfm.200700973.

[73] Y. Yin, J. Liu, Z. Wu, T. Zhang, and Z. Li, “ZIF-8 calcination derived Cu2O-ZnO* material for enhanced visible-light photocatalytic performance,” *New Journal of Chemistry*, vol. 45, no. 6, pp. 3095–3101, Feb. 2021, doi: 10.1039/d0nj05481j.

[74] W.-J. Li, E.-W. Shi, Y.-Q. Zheng, and Z.-W. Yin, “Hydrothermal preparation of nanometer ZnO powders.”

[75] H. Z. Asl and S. M. Rozati, “Structural, morphological, electrical, optical, and photoluminescence properties of spray-deposited ZnO thin film: effect of hydrochloric and acetic acids in the precursor,” *Journal of Materials Science: Materials in Electronics*, vol. 31, no. 3, pp. 2537–2543, Feb. 2020, doi: 10.1007/s10854-019-02790-z.

[76] M. Cho, H. Chung, W. Choi, and J. Yoon, “Linear correlation between inactivation of E. coli and OH radical concentration in TiO2 photocatalytic disinfection,” *Water Res*, vol. 38, no. 4, pp. 1069–1077, 2004, doi: 10.1016/j.watres.2003.10.029.

[77] A. L. Linsebigler, G. Lu, and J. T. Yates, “Photocatalysis on TiOn Surfaces: Principles, Mechanisms, and Selected Results,” 1995.

[78] Y. Du, M. S. Zhang, J. Hong, Y. Shen, Q. Chen, and Z. Yin, “Structural and optical properties of nanophase zinc oxide,” *Appl Phys A Mater Sci Process*, vol. 76, no. 2, pp. 171–176, Feb. 2003, doi: 10.1007/s003390201404.

[79] B. Lavina, P. Dera, and R. T. Downs, “Modern X-ray diffraction methods in mineralogy and geosciences,” in *Spectroscopic Methods in Mineralogy and Materials Sciences*, De Gruyter, 2014, pp. 1–31. doi: 10.2138/rmg.2014.78.1.

[80] P. F. Fewster and N. L. Andrew, “Absolute Lattice-Parameter Measurement,” 1995.

[81] D. Balzar *et al.*, “Size-strain line-broadening analysis of the ceria round-robin sample,” *J Appl Crystallogr*, vol. 37, no. 6, pp. 911–924, Dec. 2004, doi: 10.1107/S0021889804022551.

[82] H. Du, F. Yuan, S. Huang, J. Li, and Y. Zhu, “A new reaction to ZnO nanoparticles,” *Chem Lett*, vol. 33, no. 6, pp. 770–771, Jun. 2004, doi: 10.1246/cl.2004.770.

[83] P. M. Aneesh, K. A. Vanaja, and M. K. Jayaraj, “Synthesis of ZnO nanoparticles by hydrothermal method,” in *Nanophotonic Materials IV*, SPIE, Sep. 2007, p. 66390J. doi: 10.1117/12.730364.

[84] Miao. Cai, Daoguo. Yang, Keyun. Bi, Institute of Electrical and Electronics Engineers., P. & M. T. Society. Components, and Zhongguo dian zi xue hui., *Proceedings, 2012 13th International Conference on Electronic Packaging Technology & High Density Packaging (ICEPT-HDP 2012) : location, Guilin Bravo Hotel, Guilin, China : dates, Monday, Aug. 13 to Thursday, Aug. 16, 2012*. IEEE, 2012.

[85] K. Edalati, A. Shakiba, J. Vahdati-Khaki, and S. M. Zebarjad, “Low-temperature hydrothermal synthesis of ZnO nanorods: Effects of zinc salt concentration, various solvents and alkaline mineralizers,” *Mater Res Bull*, vol. 74, pp. 374–379, Feb. 2016, doi: 10.1016/j.materresbull.2015.11.001.

[86] D. Ahmed, M. Osman, and M. Abbas Mustafa, “Synthesis and Characterization of Zinc Oxide Nanoparticles using Zinc Acetate Dihydrate and Sodium Hydroxide,” 2015. [Online]. Available: http://www.aiscience.org/journal/jnnhttp://creativecommons.org/licenses/by-nc/4.0/

[87] S. Yurdakal, C. Garlisi, L. Özcan, M. Bellardita, and G. Palmisano, “(Photo)catalyst characterization techniques: Adsorption isotherms and BET, SEM, FTIR, UV-Vis, photoluminescence, and electrochemical characterizations,” in *Heterogeneous Photocatalysis: Relationships with Heterogeneous Catalysis and Perspectives*, Elsevier, 2019, pp. 87–152. doi: 10.1016/B978-0-444-64015-4.00004-3.

[88] F. Xie *et al.*, “Highly sensitive electrochemical detection of Hg(II) promoted by oxygen vacancies of plasma-treated ZnO: XPS and DFT calculation analysis,” *Electrochim Acta*, vol. 426, Sep. 2022, doi: 10.1016/j.electacta.2022.140757.

[89] L. W. Yang, X. L. Wu, T. Qiu, G. G. Siu, and P. K. Chu, “Synthesis and magnetic properties of Zn1-xCoxO nanorods,” *J Appl Phys*, vol. 99, no. 7, Apr. 2006, doi: 10.1063/1.2188031.

[90] X. Xue, R. L. Penn, E. R. Leite, F. Huang, and Z. Lin, “Crystal growth by oriented attachment: Kinetic models and control factors,” *CrystEngComm*, vol. 16, no. 8, pp. 1419–1429, Feb. 2014, doi: 10.1039/c3ce42129e.

[91] J. Ramirez-Vick *et al.*, “Cytotoxic studies of PEG functionalized ZnO Nanoparticles on MCF-7 cancer cells,” 2011. [Online]. Available: https://www.researchgate.net/publication/326541222

[92] M. Sudha, S. Senthilkumar, R. Hariharan, A. Suganthi, and M. Rajarajan, “Synthesis, characterization and study of photocatalytic activity of surface modified ZnO nanoparticles by PEG capping,” *J Solgel Sci Technol*, vol. 65, no. 3, pp. 301–310, Mar. 2013, doi: 10.1007/s10971-012-2936-y.

[93] F. Mohammad, I. B. Bwatanglang, H. A. Al-Lohedan, J. P. Shaik, H. H. Al-Tilasi, and A. A. Soleiman, “Influence of Surface Coating towards the Controlled Toxicity of ZnO Nanoparticles In Vitro,” *Coatings*, vol. 13, no. 1, Jan. 2023, doi: 10.3390/coatings13010172.

[94] B. W. Hoogendoorn *et al.*, “Ultra-low Concentration of Cellulose Nanofibers (CNFs) for Enhanced Nucleation and Yield of ZnO Nanoparticles,” *Langmuir*, vol. 38, no. 41, pp. 12480–12490, Oct. 2022, doi: 10.1021/acs.langmuir.2c01713.

[95] M. Bagherzadeh, N. Rabiee, Y. Fatahi, and R. Dinarvand, “Zn-rich (GaN)1−x(ZnO)x: a biomedical friend?,” *New Journal of Chemistry*, vol. 45, no. 8, pp. 4077–4089, Feb. 2021, doi: 10.1039/d0nj06310j.

[96] S. Dutz *et al.*, “Hybrid nanomaterials of biomolecule corona coated magnetic nanoparticles and their interaction with biological systems,” *Physical Sciences*

Reviews, vol. 7, no. 11, pp. 1311–1344, Nov. 2022, doi: 10.1515/psr-2019-0110.

[97] R. Azari, H. R. Rezaie, and A. Khavandi, "Effect of titanium dioxide intermediate layer on scratch and corrosion resistance of sol–gel-derived HA coating applied on Ti-6Al-4V substrate," *Prog Biomater*, vol. 10, no. 4, pp. 259–269, Dec. 2021, doi: 10.1007/s40204-021-00169-0.

[98] F. Heidari *et al.*, "3D construct of hydroxyapatite/zinc oxide/palladium nanocomposite scaffold for bone tissue engineering," *J Mater Sci Mater Med*, vol. 31, no. 10, Oct. 2020, doi: 10.1007/s10856-020-06409-2.

[99] V. P. Padmanabhan, R. Kulandaivelu, D. Santhana Panneer, S. Vivekananthan, S. Sagadevan, and J. Anita Lett, "Microwave synthesis of hydroxyapatite encumbered with ascorbic acid intended for drug leaching studies," *Materials Research Innovations*, vol. 24, no. 3, pp. 171–178, Apr. 2020, doi: 10.1080/14328917.2019.1624940.

CURRICULUM VITAE

Personal Information

Name, SURNAME: Muhammed EL ACCEN

Education

Bachelor degree in Materials Science and Engineering Department, Aleppo University – Syria (Graduation Year: 2015) (Graduation Project: Materials Used in Solar Systems: Properties and Improvement Processes)

Work Experience

- Monitoring and Evaluation Officer at Bonyan NGO – Idleb - Syria (Aug 2016 – Dec 2019)
- Quality Assurance Coordinator at Business Insight Company – Gaziantep - Türkiye (Jan 2020 – Mar 2022)
- Monitoring, Evaluation, Accountability, and Learning Coordinator at Bonyan NGO – Gaziantep – Türkiye (Apr 2022 – Sep 2023)
- Monitoring, Evaluation, Accountability, and Learning Manager at Bonyan NGO – Gaziantep – Türkiye (Oct 2023 – now)